3 Moist Convection and Moist Radiative-Convective Equilibrium

3.1 Convective clouds and mesoscale organization

We have seen that the irreversible formation, fallout, and partial or total re-evaporation of precipitation completely transforms the nature of moist convection so that ascending air is generally saturated and contains condensed water, while the air in between clouds is mostly unsaturated and would descend dry adiabatically were it not for radiative cooling. Air also descends in unsaturated downdrafts cooled by the evaporation of precipitation falling through them, as illustrated in Figure 2.19. The dry stratification of the atmosphere and the relatively small rates of radiative cooling keep the subsidence velocity given by (2.83) small…less than $1 cm s^{-1}$. For reasons we will return to, the convective updraft velocities are about two orders-of-magnitude stronger, so that the fractional area covered by convective updrafts implied by (2.84) is of the order of 10^{-2}. The small fraction of the sky covered by convective clouds in the tropics can be seen in the photograph in Figure 3.1

Figure 3.1: Spectrum of tropical cumulus clouds photographed from the International Space Station.

The rich tapestry of clouds visible in Figure 3.1 range from the barely visible shallow, non-precipitating clouds to cumulonimbi that span the depth of the troposphere, crowned by icy stratiform anvil clouds that spread out at or near the tropopause. These cumuli are responsible for most of the vertical transport of water, aerosols, and trace gases, and almost all of the non-radiative energy transport in the tropical atmosphere above a thin, sub-cloud layer. Their small

size – ranging from a few hundred meters to perhaps 10 km – render them unresolvable by global models, posing an immense challenge to representing their effects in such models.

The isolation of many of the convective towers in Figure 3.1 (though there are some clusters) is associated with large gradients of water concentration along their lateral boundaries. The plumes themselves are fully turbulent, and the turbulent eddies mix air from just outside the clouds into the clouds themselves, a process known as *entrainment*. This introduces large inhomogeneity in the thermodynamic properties within the cloud boundaries, which strongly affects buoyancy as well as the cloud microphysical properties that control the formation, fallout, and partial re-evaporation of precipitation. Mixing of cloudy air with unsaturated air can lead to mixtures that are colder than either of the two original samples, an outcome that is not possible in dry convection, and leads to downdrafts within the cloud. In fact, the net latent heating integrated over the volume and life cycle of a non-precipitating cumulus cloud must be zero. The net convective heating, from (2.83) combined with (2.85) and assuming that $\sigma << 1$, is given by

$$c_p M \frac{T}{\theta} \frac{d\theta}{dz},$$

and since the stratification $d\theta / dz$ is always non-negative, M must have both positive and negative values. In reality, the net convective mass flux is downward near the tops of non-precipitating and weakly precipitating cumulus clouds, and positive elsewhere.

Thus entrainment is an essential aspect of moist convection and greatly enriches the problem of understanding how convection operates. The irreversible mixing across cloud boundaries, coupled with the fallout of precipitation, is the dominant source of irreversible entropy production in the tropical atmosphere and perhaps for the whole planet (Pauluis and Held, 2002).

Early attempts to model the entrainment process were based on similarity theory of Schmidt (1941) as extended by Morton et al. (1956), which was developed to describe convection originating from sustained or instantaneous point sources of buoyancy and found to provide excellent descriptions of laboratory plumes and real convection from limited sources, such as volcanic plumes. Simple dimensional reasoning yields an expression for the upward increase in plume mass flux:

$$\frac{dM}{dz} = \alpha \frac{M}{z}, \tag{3.1}$$

where α was estimated to be $\frac{5}{3}$ from laboratory experiments. Similarly, the plumes were both predicted and observed to be conical in shape, with $r = \frac{6}{5}\alpha z$. The entrained air dilutes the buoyancy of the plume and also directly slows down the updraft as the entrained air must be accelerated to the plume velocity.

Unfortunately, cumulus clouds are not observed to be very similar to entraining plumes, as they do not originate from highly localized sources and, unlike classical plumes, can experience buoyancy reversal from entrainment. They are not observed to have conical shapes and the air within them is far more inhomogeneous than classical plumes (Paluch, 1979). Nevertheless,

moist convection continues to be modeled as modified convective plumes, using a variant of (3.1):

$$\frac{dM}{dz} = \lambda M, \tag{3.2}$$

where λ is called the *entrainment parameter* and is usually assumed to be constant, with an estimated value of around $0.15\,km^{-1}$ (Singh and O'Gorman, 2015).

Shallow convective clouds moisten their environments, leaving behind anomalously moist air that is favorable for the development of subsequent clouds, which will be less dilute than their predecessors. It is thus possible for a sequence of plumes to reach successively greater altitudes. The general picture of a turbulent plume ascending through a pristine, unperturbed environment may be too simple.

The dynamics of moist convective clouds are inextricably woven with the cloud microphysical processes that determine the spectrum of cloud drop sizes, the conversion of cloud water to precipitation, and the fall and partial or total re-evaporation of precipitation. Such processes are highly complex and fascinating in their own right and are the subject of an entire sub-discipline of atmospheric science; no short summary could do justice to the subject. Broadly, the initial spectrum of cloud drop sizes is largely determined by the size distribution of the aerosol particles that serve as cloud condensation nuclei. Virtually all the condensation that takes place is heterogeneous – occurring on the surfaces of liquid or solid aerosol particles rather than by spontaneous clumping of water molecules. There are usually enough cloud condensation nuclei that no particles grow by condensation alone to sizes sufficient to have terminal velocities comparable to those of the air motion. Thus other processes must be involved to convert small cloud water droplets or ice crystals to precipitation-size particles.

Two quite different cloud microphysical processes produce precipitation. When ice crystals coexist with liquid water droplets, the is a rapid flux of vapor from the liquid droplets to the ice crystals, since the saturation vapor pressure over ice is less than that over liquid water at the same temperature. This is known as the Wegener-Bergeron-Findeisen process, named after the scientists[1] who proposed that it could produce precipitation. Rain can also form by stochastic coalescence of liquid water droplets owing to their differential fall speeds and, to some extent, as a result of small-scale turbulent motions of the air in which they are embedded. Greater rates of collision occur with broader drop size distributions, which in turn occur with broader cloud condensation nuclei size distributions.

Observed distributions of liquid water drop sizes in precipitating cumulus clouds are strongly bimodal, with largely separate populations of cloud droplets, whose terminal velocities are small compared to air motions, and raindrops that are falling at appreciable speeds.

[1] Alfred Wegener, the German meteorologist credited with founding the theory of continental drift, was also the first to propose the thermodynamic hypothesis for precipitation formation, in 1911, and eleven years later, the Norwegian scientist Tor Bergeron discovered the process at work in the deposition of ice on cold trees immersed in fog whose temperature was above freezing. The hypothesis was further refined and extended in the 1930s by the German meteorologist Walter Findeisen.

Maritime air masses tend to have broad aerosol size distributions, owing in part to the presence of large salt particles resulting from evaporation of spray droplets, and so cumuli developing over tropical oceans tend to precipitate rather easily compared to their terrestrial counterparts, as can be seen in Figure 3.2.

Thus cloud microphysical processes have a strong bearing on the amount of latent heat release in clouds, the formation and concentration of cloud ice, and by modifying cloud drop size distributions, on the optical properties of clouds. Those who assume that the details of such processes are of secondary concern for large-scale tropical phenomena – including tropical cyclones – do so at their peril. We have already seen that the efficiency with which precipitation forms, falls out, and re-evaporates largely determines the water vapor content of RCE states, and this is just the tip of the iceberg.

Very shallow tropical cumuli do not live long enough to form precipitation size-particles, and the re-evaporation of cloud water in turn limits the vertical development of the clouds. Under conditions of strong large-scale subsidence over the ocean, shallow cumuli and/or stratocumuli – which in contrast to cumuli cover large fractions of the sky – dominate the skyscape.

But, especially over the oceans, cumuli do not have to become very deep before they precipitate. Figure 3.2 shows an example of a shallow but precipitating cumulus cloud near the Caribbean island of Barbados. A cloud of similar dimensions over a continental interior would probably not produce rain or snow.

Figure 3.2: Precipitating cumulus mediocris over the tropical Atlantic near Antigua. The cloud is a few kilometers in horizontal and vertical size.

Although precipitation from shallow cumuli over tropical oceans is usually quite light, evaporation is enough to cause downdrafts and cold pools in the subcloud layer and these make beautiful patterns in space-based images, an example of which is shown in Figure 3.3. The black, nearly cloud-free patches represent cold pools produced by evaporation of rain from shallow cumuli. These spread out in the subcloud layer and often produces arcs of cumuli at their edges. The clouds that produced the cold pools in most places have vanished before the

time of the image, reminding us that while the pattern of clouds pay persist for many days, each individual cloud has a lifetime of a few tens of minutes.

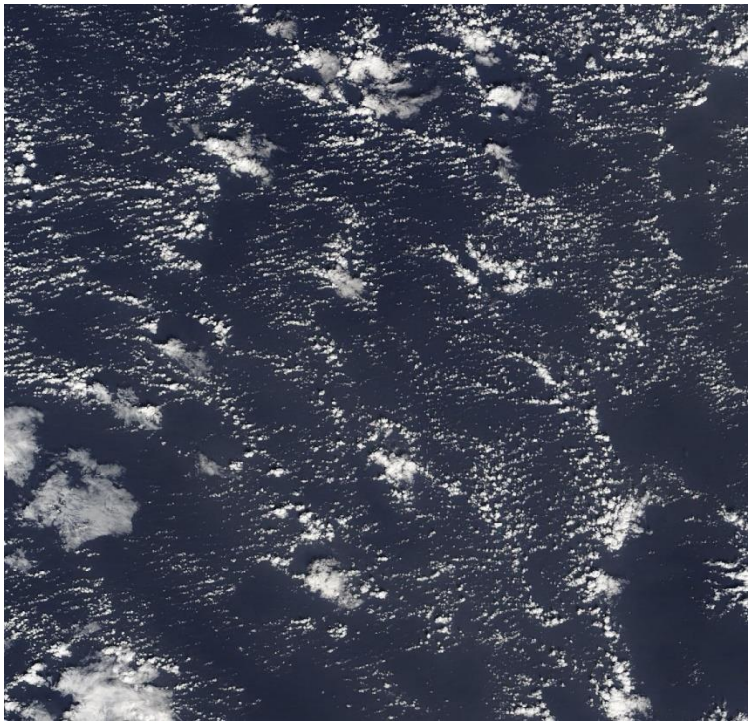

Figure 3.3: Patterns in shallow cumuli over the tropical Atlantic as observed by NASA's MODIS/Aqua on December 19th, 2013.

Deep cumulonimbi can span the whole depth of the troposphere and occasionally overshoot into the lower stratosphere, where they are important agents for injecting water and other tropospheric tracers into the stratosphere. Figure 3.4 shows an example of a tropical cumulonimbus as seen from the International Space Station.

Figure 3.4: Cumulonimbus over western equatorial Africa as captured from the International Space Station on February 5, 2008.

Deep convection is often organized into clusters and squall lines, or arcs, as can be seen in figure 3.5. Evaporation of falling precipitation drive strong downdrafts, which spread out as density currents in the boundary layer. In the presence of low-level shear, deep convection redevelops on the downshear side of the spreading cold pools by a mechanism elucidated by Thorpe et al. (1982) and by Rotunno et al. (1988). Potentially buoyant air approaches the squall line from the downshear side, carrying horizontal vorticity associates with the ambient low-level wind shear. The vorticity vector is approximately parallel to the edge of the cold pool. When the air encounters the edge of the cold pool, the baroclinic generation of vorticity tends to decrease this vorticity, so that the air forced up over the cold pool emerges from the boundary layer with little vorticity, favoring an upright updraft. A schematic cross-section through a squall line is shown in Figure 3.6.

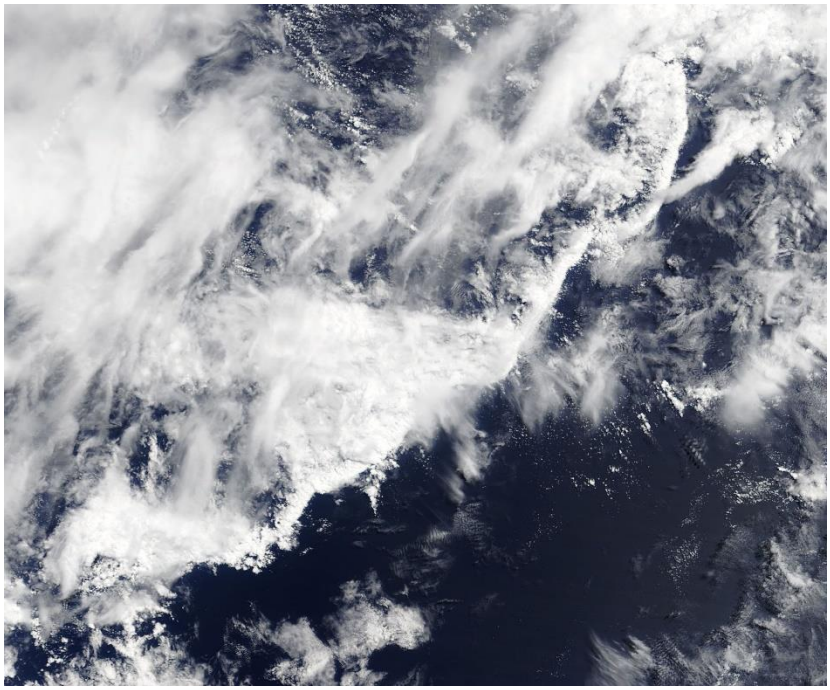

Figure 3.5: A tropical squall line over the western tropical North Pacific on August 14th, 2018. The entire system spans about 400 km from southwest to northeast.

Low level air approaches from the right, or downshear side of the system: Its vorticity is directed into the page. As it encounters the leading edge of the cold pool, it suffers a decrease in vorticity and is forced upward over the cold pool, then rising buoyantly through deep cumulonimbi. Individual deep convective cells form this way and are swept back (to the left) by the squall line-relative flow, decaying as they go. Cloud particles are also swept leftward near the top of the squall line; these settle downward, melting as they cross the freezing level. The cooling produced by melting and evaporation drive a mesoscale downdraft and rear inflow. The cells that make up the squall line have typical lifetimes of 30-45 minutes while the squall line itself may last many hours.

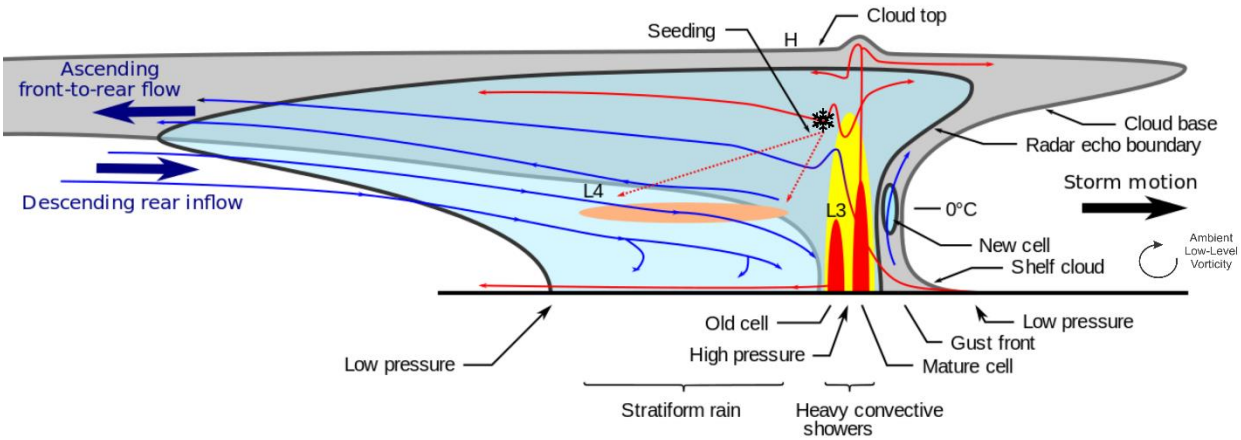

Figure 3.6: Schematic cross-section through a squall line. The cross-section spans about 100 km in the horizontal and 15 km in the vertical.

Squall lines represent a mode of organization brought about by the interaction of deep convection with environmental shear flow. Deep convection can also self-organize by modulating radiative and surface fluxes, forming clusters of deep convective clouds. If they occur sufficiently far from the equator they can begin to rotate, developing into tropical cyclones. We will have much more to say about this, but for now Figure 3.7 shows an example of such a cluster. The cluster contains around 10 individual cumulonimbi at this time, and once can see shallow cumuli forming at the leading edge of a gust front on the near side. The atmosphere around the cluster is unusually free of convection.

Figure 3.7: Cluster of thunderstorms over the floodplain of the Brahmaputra River near the India-Bangladesh border, July 31st 1985, photographed from the space shuttle Challenger.

Overall, the depth of cumulus clouds in the tropics has a tri-modal distribution, as illustrated in Figure 3.8. There are many shallow cumuli, some congesti (reaching to the middle troposphere around the freezing level), and a few deep cumulonimbi spanning the depth of the troposphere. The spectrum is, of course, continuous but does seem to exhibit these three peaks; one can see a suggestion of this in Figure 3.1. Here there are many shallow cumuli in the foreground, interspersed with some cumulus congestus clouds. Deep cumulonimbi dominate the background. Although the deep cumulonimbi are few and far in between, they are responsible for most of the rainfall in the warmer parts of the tropics.

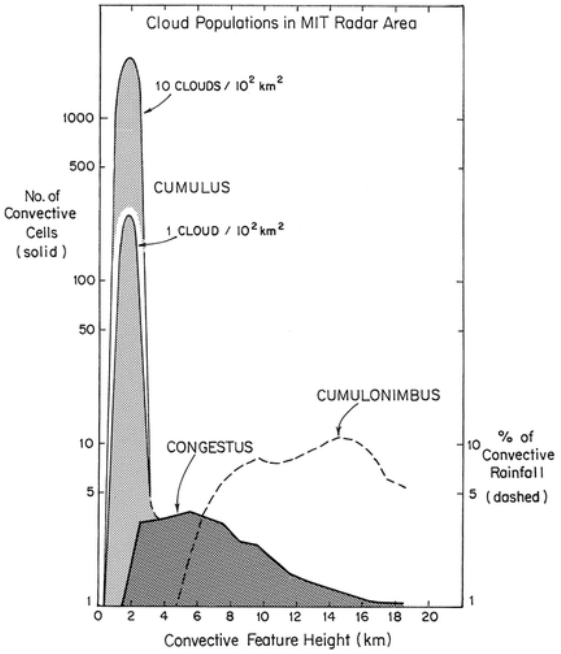

Figure 3.8: Average number of clouds over a region of the tropical South Pacific (solid curves) and percent of convective rainfall (dashed curve) as a function of convective feature height.

Convective rainfall has distinct diurnal cycles. Over the sea, rainfall tends to peak in the hours just before sunrise, while over land the peak occurs in the late afternoon or early evening. Surface fluxes over the sea do not usually show strong diurnal variations owing to the large heat capacity of the ocean's mixed layer, but during the day, direct absorption of sunlight in the atmosphere, mostly by water vapor, leads to a reduction in the net radiative cooling rate and therefore of the net rate of destabilization to convection. Thus convective forcing is maximum during the night. Over land, on the other hand, the very low heat capacity and thermal conductivity of most soils yields surface fluxes that are nearly in balance with the net (solar and infrared) radiative forcing of the surface, which peaks around noon, local time. Thus the rate of destabilization peaks in the middle of the day, and this peak is far stronger than the oceanic nocturnal maximum of destabilization.

As we will see in the next subsection, the time scale over which convection removes instability is not very short compared to a day, so the response of the convection lags the forcing, explaining the ocean convective peak around sunrise and the land peak near sunset. The much stronger diurnal forcing over the land coupled with the lag of the convective response allows somewhat more instability to build up, yielding stronger convection. This is evident in a global map of lightning detected from space presented in Figure 3.9. Lightning is almost exclusively a terrestrial phenomenon, with very little activity over the sea. Strong peaks are evident over equatorial Africa and the mountainous regions of northeastern Columbia and far western Venezuela.

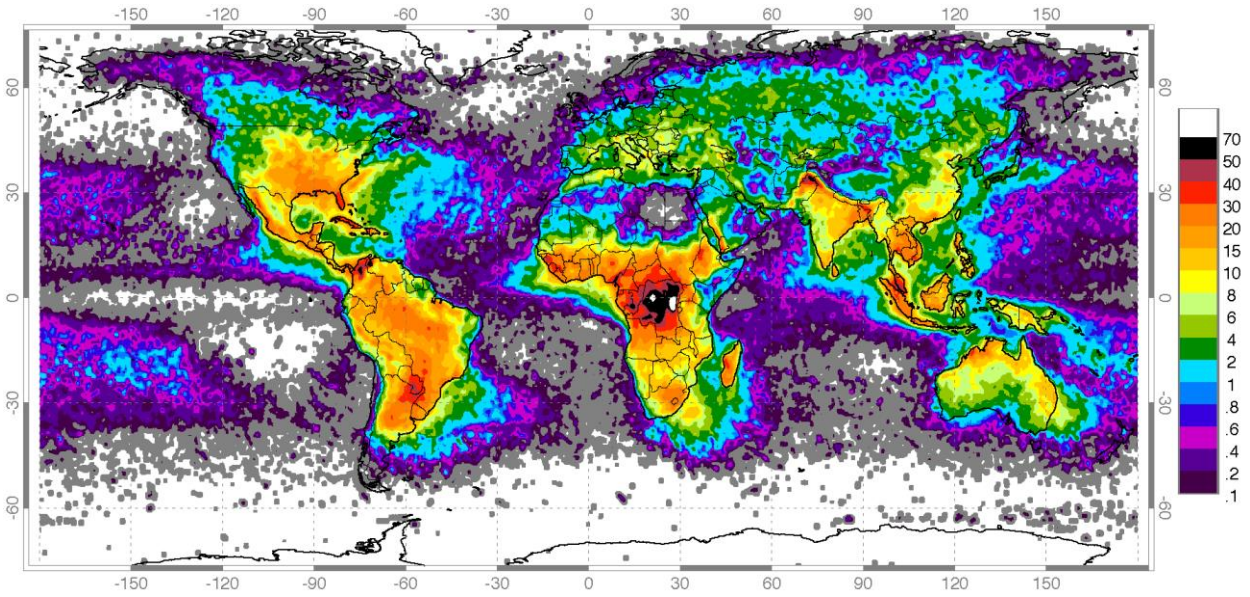

Figure 3.9: Global lightning flash rate, in flashes km^{-2} yr^{-1}. Data obtained from April 1995 to February 2003 from NASA's Optical Transient Detector and from January 1998 to February 2003 from NASA's Lightning Imaging Sensor.

3.2 Moist convective stability and the tropical tropospheric lapse rate

Entrainment and the irreversible fallout and partial re-evaporation of precipitation complicates the assessment of stability of an atmosphere to moist convection. The presence of saturated and unsaturated air at the same pressure level means that the buoyancy of saturated air, with respect to the surrounding unsaturated air, cannot be expressed as a function of pressure and just one other variable; a third variable is required. For this reason, the stability of an unsaturated atmosphere to moist convection cannot be expressed in terms of the vertical gradient of a single variable, a fact that turns out to have profound consequences for the atmosphere.

Here it proves easier to work with a different entropy variable called the *saturation entropy*, denoted by the symbol $s*$. It is the entropy air would have were it saturated at the same temperature and pressure. From (2.69) its definition is then

$$s^* \equiv \left(c_{pd} + r_t c_l\right)\ln\left(\frac{T}{T_0}\right) - R_d \ln\left(\frac{p_d}{p_0}\right) + \frac{L_v r^*}{T} + c_l r_t, \tag{3.3}$$

where $r*$ is the saturation mixing ratio. It is important to note that $s*$ is not conserved, except when the air is saturated, in which case it is identical to the ordinary entropy, s. But $s*$ is a state variable, which is important to what follows. The last term in (3.3) is unnecessary, but makes further derivations a little more compact. As entropy is arbitrary to within and additive constant, which can be a conserved variable, (3.3) is still conserved in reversible processes in saturated air.

Using the chain rule, we can express small fluctuations of specific volume at constant pressure as

$$\alpha' = \left(\frac{\partial \alpha}{\partial s*}\right)_{p,r_t} s*' + \left(\frac{\partial \alpha}{\partial r_t}\right)_{p,s*} r_t', \tag{3.4}$$

where we have chosen total water mixing ratio, r_t, to be the third variable. Using (2.69) and (2.71) we can write

$$dk = Tds* - c_l T \ln\left(\frac{T}{T_0}\right) dr_t + \alpha\left(1 + r_T\right) dp, \tag{3.5}$$

where, in the last term, we have assumed that the total water content is equal to the vapor content in unsaturated air. By using (2.73), and a similar identity:

$$\left(\frac{\partial}{\partial r_t}\right)_{p,s*}\left(\frac{\partial k}{\partial p}\right)_{s*,r_t} = \left(\frac{\partial}{\partial p}\right)_{s*,r_t}\left(\frac{\partial k}{\partial r_t}\right)_{p,s*}, \tag{3.6}$$

and using (3.5), we have

$$\left(\frac{\partial \alpha}{\partial s*}\right)_{p,r_t} = \frac{1}{1 + r_t}\left(\frac{\partial T}{\partial p}\right)_{s*,r_t},$$

which is the same as (2.74) but in terms of saturation entropy, and

$$\left(\frac{\partial \alpha}{\partial r_t}\right)_{p,s*} = \frac{1}{1 + r_t}\left[-\alpha - c_l\left(\frac{\partial T}{\partial p}\right)_{s*,r_t}\left(1 + \ln\left(\frac{T}{T_0}\right)\right)\right]. \tag{3.7}$$

Using these and the hydrostatic equation in (3.4) we can write the perturbation buoyancy as

$$\begin{aligned} B = \frac{\alpha'}{\alpha} &= \frac{1}{\alpha}\left(\frac{\partial \alpha}{\partial s*}\right)_{p,r_t} s*' + \frac{1}{\alpha}\left(\frac{\partial \alpha}{\partial r_t}\right)_{p,s*} r_t' \\ &= \frac{1}{1 + r_t}\left[\Gamma_m s*' - g r_t' - \left(\Gamma_m c_l\left(\ln\left(\frac{T}{T_0}\right) + 1\right)\right) r_t'\right]. \end{aligned} \tag{3.8}$$

At first glance, it would appear that buoyancy depends on the arbitrary constant T_0, but remember that T_0 also appears in the definition of $s*$ and the two terms cancel in (3.8).

If the relation (3.4) did not do the trick, (3.8) makes it clear that to calculate buoyancy one needs to know not just the difference between the saturation entropies of the parcel to be lifted and its environment, but the difference between the water contents of the parcel and environment as well. *Knowing the vertical profile of s or $s*$ does not suffice to determine the stability of an atmosphere to a moist process*.

Even if one neglects the condensed water in clouds, the contribution of water vapor to density is significant enough to make the contribution of r_t' important in (3.8). Thus it is not possible to

make quantitatively accurate estimates of the buoyancy of parcels lifted by some adiabatic process using two-dimensional diagrams such as skew-T-log-p charts (e.g. Figure 2.18).

Fortunately, the easy numerical computation of thermodynamic processes renders thermodynamic diagrams unnecessary, though they are still useful for plotting the results of such computations.

As an illustration, let's travel to the beautiful island of Majuro, part of the Marshall Islands of the tropical North Pacific. Rawinsondes (weather balloons) are launched twice daily from this small coral atoll, as they are from many stations around the world[2]. Instruments suspended from the ascending balloons measure pressure, temperature, relative humidity, and GPS location, from which the balloon drift and thus the horizontal winds can be inferred.

Figure 3.10 is a variant on the classical skew-T-log-p chart in which isopleths of constant density temperature, T_ρ, are plotted instead of isotherms.

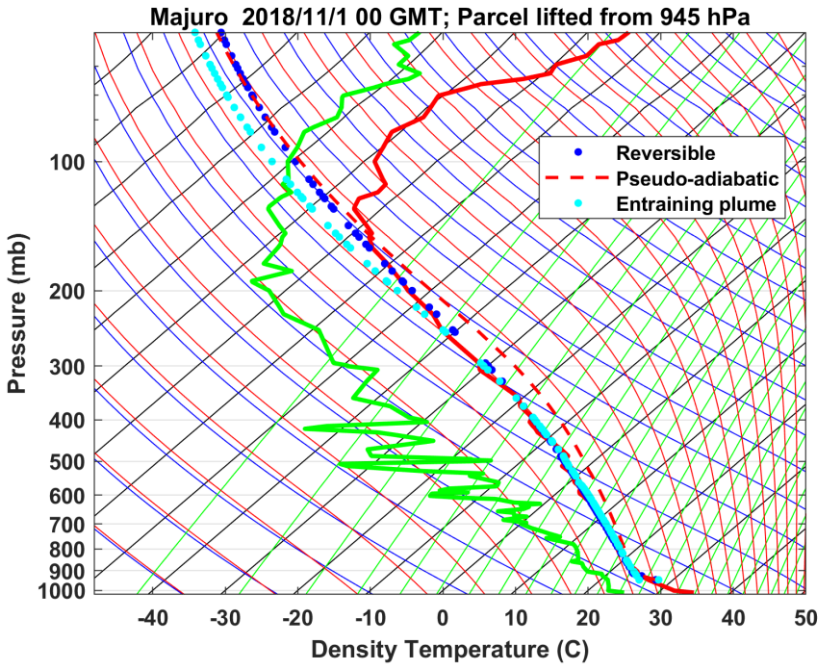

Figure 3.10: Skew-T_ρ – log-p diagram similar to the thermodynamic diagram in Figure 2.18, except that the density temperature replaces the actual temperature. The thin solid red curves are virtual pseudo-adiabats, showing the virtual temperature of air displaced pseudo-adiabatically. The thick, solid red and green curves show the virtual temperature and dew point temperature recorded by the rawinsonde launched from Majuro at 00 GMT, November 1st 2018. See text for a description of the other curves.

The *density temperature* is defined as the actual temperature a perfectly dry sample of air would have if it had exactly the same density as the actual, moist sample (which may also contain suspended condensed water). It is given by

[2] For a map of active rawinsonde stations, see the web site maintained by the University of Wyoming: http://weather.uwyo.edu/upperair/sounding.html

$$T_\rho \equiv T\left[\frac{1+r/\epsilon}{1+r_t}\right], \tag{3.9}$$

where r is the mixing ratio, r_t is the total water content, and ϵ is the ratio of the molecular weight of water to a suitably defined weighted mean molecular weight of the other constituents of the atmosphere. (It has a value of about 0.622 in our atmosphere.) If there is no condensed water in a sample, its density temperature is the same as its *virtual temperature*, T_v:

$$T_v \equiv T\left[\frac{1+r/\epsilon}{1+r}\right]. \tag{3.10}$$

The thick, solid red and green curves in Figure 3.10 show the virtual temperature and dew point temperature recorded by the rawinsonde launched from Majuro at 00 GMT, November 1st 2018. The thick red dashed curve shows the density temperature of a sample of air lifted pseudo-adiabatically from 945 hPa (one of the sample points in the sounding) and the dark blue dots show the density temperature of a sample lifted reversibly (i.e. not allowing any condensed water to fall out) and without freezing, from the same starting pressure. The light blue dots in the figure show the virtual temperature of a sample lifted from the same level, but allowing for both entrainment of undisturbed environmental air, and latent heat of fusion when water vapor condenses directly into ice crystals (which are then removed, after entrainment, according to the pseudo-adiabatic process.) The entrainment constant used here (see equation 2.92) is 0.18, about an order-of-magnitude smaller than deduced from laboratory experiments (Morton et al., 1956).

Once can see in Figure 3.10 that air lifted from about 945 hPa (roughly 500 m over the sea surface) through the depth of the troposphere by a pseudo-adiabatic process has appreciable buoyancy up to about 180 hPa, but the same sample lifted by either a reversible process (in which the condensed water contributes to the effective density of the lifted air) or as an entraining plume with freezing has little buoyancy. This is made more apparent in Figure 3.11, which simply graphs the difference between the lifted sample and environmental density temperatures of this sounding, for the three aforementioned processes.

We mention here two other ways of characterizing the stability of soundings. The first begins by defining a new quantity, the *buoyancy entropy*, or s_B. This is simply defined as the reversible entropy that a hypothetical saturated sample with no condensed water would have to have at some reference pressure such that, when lifted reversibly (with no freezing), it would have the same density temperature as the air at a given pressure. That is, at each level in the sounding, we find that value of reversible entropy at a reference pressure, p_0, that, when lifted to the given level, has the same density temperature as the virtual temperature at that level. We then define the *buoyancy potential temperature*, θ_B, as

$$\theta_B \equiv 300\,\mathrm{e}^{s_B/c_p}, \tag{3.11}$$

where c_p is the heat capacity of dry air at constant pressure, and the factor 300 is an arbitrary constant. It is important to note that with these quantities, *the reference pressure matters*! It is not arbitrary. It should be chosen as a level typical of where air ascending in cumulus clouds

first becomes saturated when lifted from the subcloud layer. In what follows, we choose it to be the lifted condensation level of air at the lowest level in the soundings.

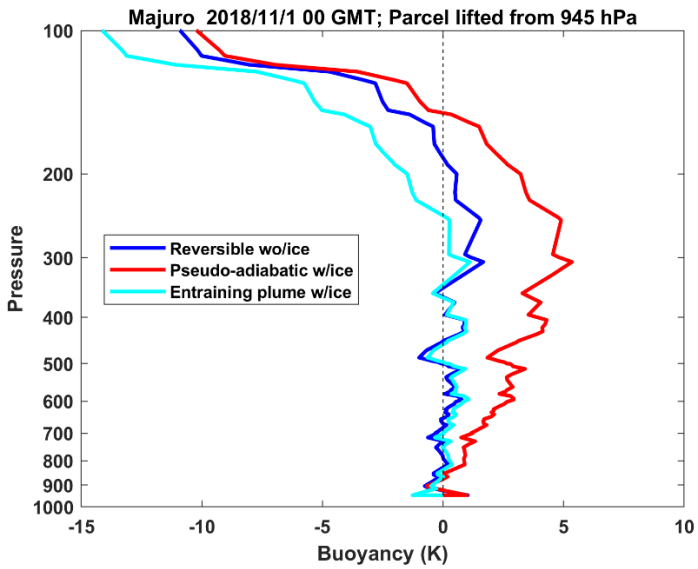

Figure 3.11: Difference between the density temperatures of a sample lifted from 945 hPa by three processes, and the environmental density temperature for the same sounding displayed in Figure 3.10.

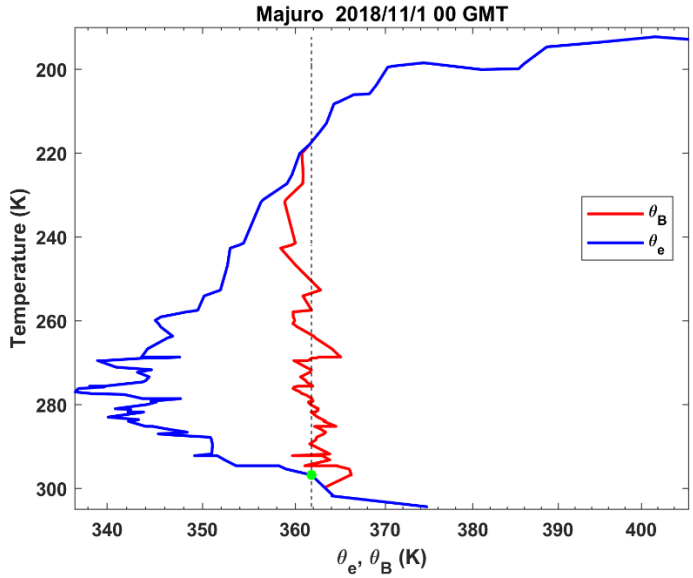

Figure 3.12: The buoyancy potential temperature, θ_B (red), of the sounding shown in Figure 3.10, compared to the equivalent potential temperature (θ_e, blue). The green dot indicates the 945 hPa level. Note that the ordinate here is absolute temperature and the abscissa is in equal increments of the logarithm of potential temperature.

Note that θ_B is conserved under reversible adiabatic displacements.

Figure 3.12 shows, in red, the buoyancy potential temperature graphed against absolute temperature and compared to the equivalent potential temperature, θ_e, defined as

$$\theta_e \equiv 300e^{s/c_p}, \tag{3.12}$$

where the entropy, s, is given by (2.69). This is for the same sounding as that used in Figures 3.10-3.11. A sample lifted from about 945 hPa in this case has roughly the same θ_B as its environment, rendering it nearly neutrally buoyant, consistent with the blue curve in Figure 3.11. We have plotted θ_B against absolute temperature rather than pressure, and in the abscissa in Figure 3.12 is in equal increments of $\ln(\theta_B)$. The reason for doing this will become apparent shortly.

A more comprehensive evaluation of stability can be accomplished using a buoyancy diagram of the type shown in Figure 3.13. Here we simply calculate the difference between density temperature of samples lifted from all levels of the sounding to all levels, and contour the difference. The ordinate is the logarithm of the pressure to which the sample is lifted, and the abscissa is the pressure from which the parcel is lifted. Figure 3.13 is for reversible adiabatic displacements (dry adiabatc to the lifted condensation level, and moist adiabatic thereafter) but the concept can be applied to any parcel lifting process.

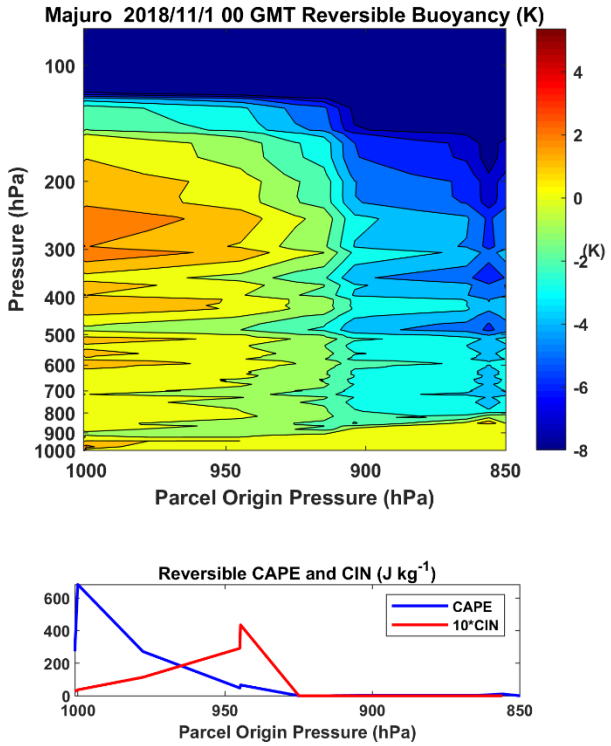

Figure 3.13: Top: Buoyancy matrix, showing the difference between the density temperatures of parcels lifted by a reversible, ice-free moist adiabatic process and that of their environment, using the same sounding as in Figures 3.10-3.12. The abscissa shows the origin pressures of the lifted parcels and the ordinate the pressures to which the parcels are lifted. Bottom: The CAPE and CIN of parcels lifted to their levels of neutral buoyancy (see text for explanation).

The stability of vertical profiles to moist processes can be compactly summarized by the two vertically integrated quantities: The *Convective Available Potential Energy* ($CAPE_i$), and the *Convective Inhibition* (CIN_i). $CAPE_i$ is the work per unit mass done by a parcel lifted from its origin level *i* to *its level of neutral buoyancy*, LNB_i. The latter is the highest level in the sounding at which the lifted parcel's buoyancy vanishes. If we follow the parcel from its origin level i up to LNB_i and then back down in the adjacent undisturbed environment, the work done is given by

$$CAPE_i = -\oint \alpha dp = \int_{LNB_i}^{i} R_d \left(T_{\rho p} - T_{\rho e}\right) d\ln(p), \tag{3.13}$$

where $T_{\rho p}$ is the density temperature of the lifted parcel and $T_{\rho e}$ that of its environment. The $CAPE_i$ of the Majuro sounding is shown as a function of the parcel origin level i in the bottom panel of Figure 3.13 (blue curve). The blue curve in the bottom panel is simply the vertical integral of the quantity contoured in the top panel of Figure 3.13. The $CAPE_i$ of the parcel originating at 945 hPa is also proportional to the area between the colored curves and the vertical dashed black line in Figure 3.11.

The convective inhibition of a parcel i, CIN_i, is defined as the work needed to lift a parcel from its origin pressure to its *Level of Free Convection*, LFC_i., which is usually defined as the lowest level at which a lifted parcel achieves positive buoyancy. The convective inhibition is given by

$$CIN_i = -\int_{LFC_i}^{i} R_d \left(T_{\rho p} - T_{\rho e}\right) d\ln(p). \tag{3.14}$$

Note the negative sign. By definition, the integrand of (3.14) is negative, so CIN_i is defined as a positive quantity. But here we define CIN_i a bit differently as the integral from the origin level up the level of neutral buoyancy, LNB_i, but only including nonpositive values of $T_{\rho p} - T_{\rho e}$. This is because, in the tropics, there may be multiple levels at which the sign of the buoyancy reverses, causing some ambiguity in defining the convective inhibition. But when a lifted parcel has appreciable positive buoyancy through most of its ascent, the two definitions usually yield the same result. The CIN_i of the Majuro sounding is shown by the red curve in the bottom panel of Figure 3.13; here it has been multiplied by 10 to give it more visibility.

It is also possible to described stability in terms of the difference between suitably defined entropy of a lifted parcel and that of its environment. We can relate the work done on a parcel, given by (3.13), to entropy and other quantities using (2.72):

$$\begin{aligned} CAPE_i = -\oint \alpha dp &= \oint \left[Tds - c_l T \ln(\frac{T}{T_0}) dr_t + \alpha r_T dp - dk \right] \\ &\cong \oint \left[Tds - c_l T \ln(\frac{T}{T_0}) dr_T + gz dr_T \right]. \end{aligned} \tag{3.15}$$

Variations in enthalpy, k, drop out of the integral as they constitute perfect differentials, and in the small term involving pressure work on water, we have used the hydrostatic approximation:

$$\alpha r_T dp \simeq -g r_T dz = -d(g r_T z) + gz dr_T.$$

Remember that T_0 also appears in our definition of entropy, (2.69), which cancels with the middle term in (3.15). For a particular thermodynamic process, we can always define a value of T_0 that minimizes the middle term in (3.15) and we will therefore not concern ourselves with that term here except to choose a suitable value in calculating the entropy such that this term is small.

The last term in (3.15) represents the work needed to lift water.

In defining the buoyancy potential temperature, θ_B, we took into account the density temperatures of the lifted parcel and its environment. Thus, to a good approximation,

$$CAPE_i \simeq \int_{LNB_i}^{i} c_p \left(\ln \theta_{Bp} - \ln \theta_{Be} \right) dT, \tag{3.16}$$

which is proportional to the area enclosed by the red curve and the vertical dashed line in Figure 3.12, for a parcel lifted from 945 hPa. This is why we plotted the sounding in $\ln \theta_B - T$ coordinates.

Diagrams of the type displayed in Figures 3.10-3.13 can easily be made for any rawinsonde station over the last few decades using software available at the **course web site**.

The parcel origin level and the nature of the lifting process are both terribly important for defining $CAPE_i$ and CIN_i in the tropics, where buoyancies usually have small magnitude. Many research papers and textbooks are sloppy about this, referring to CAPE and CIN as though they are unique properties of a sounding, without stating the parcel origin level and without defining the lifting process. (In these cases, CAPE and CIN usually refer to pseudo-adiabatic lifting from the lowest level in the sounding.) None of the lifting processes described in this chapter perfectly capture the likely buoyancy of convective clouds, and it must always be remembered that the air within clouds, and indeed the air entering the bases of the clouds, are fully turbulent and have strongly inhomogeneous thermodynamic processes.

Figures 3.10 – 3.13 show that this particular sounding is unstable to air lifted from near the surface by any of the three processes considered. As particularly evident in Figure 3.13, the parcel buoyancy decreases as its origin height increases, with an abrupt transition to low buoyancy near 940 hPa – about 600 m above the ocean surface. As demonstrated by Xu and Emanuel (1989), the tropical atmosphere over the warmest parts of the tropics is nearly neutral to reversible ascent from just below the top of the subcloud layer (see Chapter 4 for a discussion of tropical boundary layers), to within the instrumental accuracy of rawinsonde measurements. Why this should be so remains something of a mystery. Perhaps, as hinted in Figures 3.10 and 3.11, this is because a reversible adiabat happens to lie close to the temperature of an entraining plume in which the latent heat of fusion is accounted for. Yet the latent heat of fusion, when included, must affect not only the parcel temperature but, ultimately the temperature of the environment in moist radiative-convective equilibrium (see the next section of this chapter). Since no precipitation reaches the surface in the ice phase in the tropics (except on high mountains) there can be no net release of latent heat of fusion in the column. Moreover, since freezing generally occurs at a lower temperature than melting, thanks to supercooling of cloud water, the latent heat of fusion subtracts from the work done in any closed thermodynamic cycle, so in principle latent heat of fusion should make convection weaker. This

contradicts conclusions based on considering the latent heat of fusion's effects only on lifted parcel temperature and not, ultimately, on the environment.

The condensed water content of clouds is almost everywhere much lower than that obtained by adiabatic ascent from cloud base. Yet clouds are highly inhomogeneous, and in measurements taken by slow-flying gliders, a few samples do seem to have nearly adiabatic water content (Paluch, 1979; Figure 4). It is also possible that samples that escape mixing also have a hard time forming precipitation, so that the majority of samples having sub-adiabatic water content have also been diluted by mixing, which usually decreases their buoyancy.

Whatever the reason, it remains an empirical fact that the tropical troposphere is nearly neutral to reversible ascent from near the top of the subcloud layer; that is, it has nearly constant θ_B. We will have many occasions to make use of this property through the rest of this book.

But there are several circumstances that lead to appreciable values of $CAPE_i$, defined in any reasonable way. The strong diurnal variation of surfaces fluxes on land destabilizes the atmosphere faster than convection can develop and remove the instability, so that CAPE accumulates during the day, typically reaching peak values in the late afternoon. Figure 3.14 shows a buoyancy matrix and $CAPE_i$ diagram for a sounding at Tampa, Florida at 00 GMT on September 1st, 2017. This is about an hour before sunset in Tampa at this time of year.

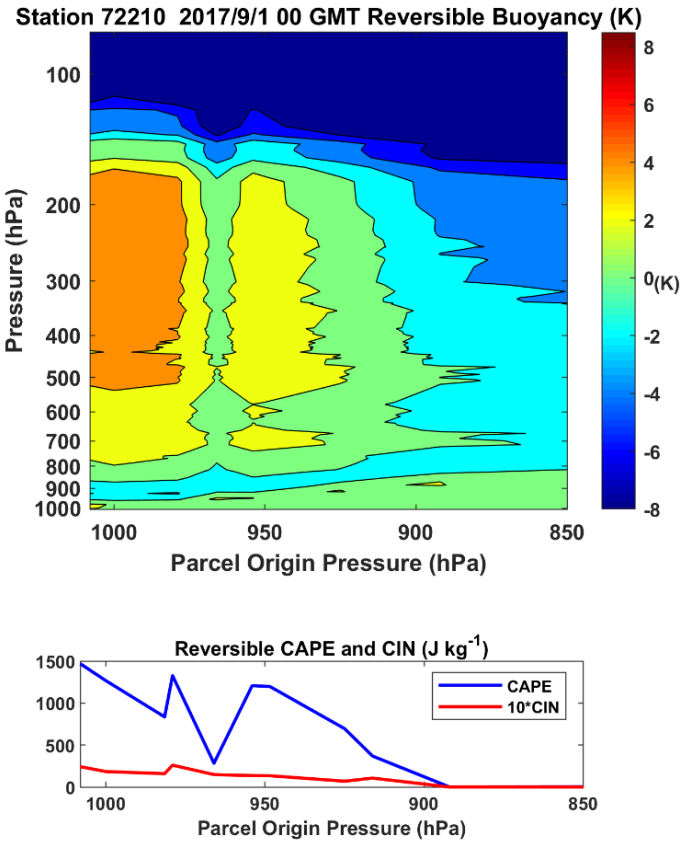

Figure 3.14: Buoyancy matrix and CAPE and CIN diagram as in in Figure 3.13, but for Tampa, Florida (USA) at 00 GMT on September 1st, 2017.

Inspection of the sounding plotted on a skew-T-log-p diagram as in Figure 3.10 shows that the temperature lapse rate in the free troposphere nearly follows the density temperature of a reversible adiabat, as in most maritime tropical soundings. But the entropy of the boundary layer is high so that large values of CAPE develop for air through the whole depth of the subcloud layer (bottom panel of Figure 3.14). Averaged over this layer, CAPE values are almost an order-of-magnitude higher than is typical for maritime soundings such as the Majuro profile in Figures 3.10-3.13. Were all of the potential energy per unit mass, quantified by CAPE, converted to kinetic energy, $50\,ms^{-1}$ updrafts would result.

Although Tampa is near the west coast of Florida, air flow during the summer is generally from the east, so that afternoon and evening thunderstorms develop over the peninsula and drift westward toward Tampa. The region around Tampa has the highest annual lightning discharge rate in the U.S. The accumulation of CAPE during daylight hours over land is almost certainly the reason for the high lightning rates seen in Figure 3.9. The charge separation that leads to lightning depends on significant lofting of large ice particles, which can only occur in sufficiently strong updrafts.

Even larger values of CAPE can build up when deep, nearly dry-adiabatic layers spawned over dry soils such as found in deserts are advected over moist air and/or moist soils. This is common over the U.S. plains during spring, when strong solar heating of the dry soils of the desert southwest and northern Mexico heats the still-chilly springtime air from below, yielding deep, dry-convecting layers. These are then advected by the still-strong westerly springtime flow over the moister soils to the east, and as water evaporates into them, the surface air is chilled and moistened. Daytime growth of a boundary layer under the desert air can result in very large values of CAPE, as illustrated by the Norman, Oklahoma sounding at 00 GMT on May 5th, 2007 (Figures 3.15 and 3.16). This sounding was made about 2 hours before sunset. Reversible CAPE values are as high as $4000\,J\,Kg^{-1}$, much larger than the unstable Tampa sounding, and the unstable air occupies a deep layer. Unlike tropical soundings, CIN values are also large and prevent any release of the instability, permitting large values of CAPE to accumulate with no convection at all. Note also in Figure 3.15 that the lapse rate of temperature in the free troposphere is somewhat steeper than a reversible adiabat, again in contrast to tropical soundings, including the Tampa sounding.

The Norman sounding illustrates a rather special circumstance under which instability builds up, contained by a potential barrier represented by large values of CIN, and may subsequently be released explosively, resulting in severe thunderstorms and attendant phenomena such as tornadoes and hail. These conditions develop when dry soils are found upwind of and close to wet soils, and where there is sufficiently strong airflow from the dry toward the moist regions. They are rare in the tropics, and we will not further concern ourselves with such conditions.

Over tropical oceans, convection – whether deep or shallow – may be considered a *quasi-equilibrium process* (Arakawa and Schubert, 1974) wherein convection releases instability at the rate it is generated by larger-scale processes such as radiative cooling of the atmosphere and surface enthalpy fluxes, much like dry convection over a heated surface or steadily boiling water in a pot. It should not be thought of as a store-release mechanism as in the Norman case illustrated above. Even over land, where diurnal surface heating is too fast for the convection to keep up with the generation of instability, one can describe the physics as a lagged-equilibrium process, where although the convective response lags the diurnally varying forcing, over longer

time scales the convection can be regarded as being in equilibrium. This is the view of convection we will adhere to throughout the remainder of this book.

3.3 Moist Radiative-Convective Equilibrium

a. General features of moist RCE

We are now in a position to extend our discussion of radiative-convective equilibrium from Chapter 2 to the case in which the convection is moist and precipitating. Moist RCE is considerably more complicated and endlessly more interesting than the dry case. While, as we have just seen, moist convection tends to establish characteristic profiles of (virtual) temperature, as in the case of dry convection, it most certainly does not mix conserved variables though the depth of the convective layer, simply because the turbulent patches of convection occupy a small factional volume of the convecting layer, thanks to the irreversible fall-out of condensed water. Thus the central challenge of understanding moist RCE, and indeed of representing cumulus convection in models in which it cannot be resolved, is getting the vertical distribution of moisture and stratiform clouds right. Since water vapor is the most important greenhouse gas in our atmosphere, and its presence above the subcloud layer in almost entirely owing to lofting of water by convection, *moist RCE is a strongly two-way process*, with radiation driving convection and convection determining the distribution of the most important greenhouse gas. Convection also determines the distribution of associated stratiform or quasi-stratiform clouds such as ice anvils and boundary-layer clouds, which greatly affect the distribution of radiative cooling.

In recent years, it has been possible to simulate moist RCE using numerical models that permit but do not come close to resolving moist convective clouds. Before turning to such models, we aim for some conceptual understanding of most RCE using very simple models.

We begin with simple RCE state in which the radiative cooling and ocean temperature are specified rather than calculated; that is, we first tackle the one-way problem. The structure of a very simple analytical model is shown in Figure 3.17. Deep, moist convective updrafts carry an upward mass flux per unit area M_u out of the boundary layer and through the density-weighted depth, H, of the troposphere. Downdrafts driven by evaporation of falling precipitation carry a mass flux M_d, and the air outside convective systems slowly subsides through the troposphere at a velocity w_e. Conservation of mass requires that

$$M_u = M_d + \rho w_e, \tag{3.17}$$

where ρ is a characteristic density of the lower troposphere. The troposphere is cooling at a constant rate given by Q_{rad}, and there is a surface enthalpy flux (dominated by a latent heat flux) given by F_s. Conservation of energy in the whole system requires that

$$F_s = Q_{rad} H. \tag{3.18}$$

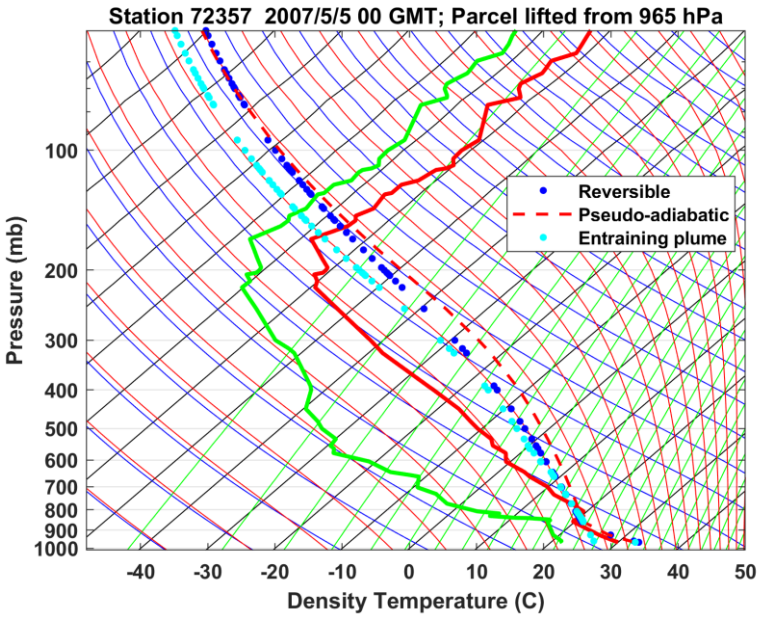

Figure 3.15: As in Figure 3.10, but for Norman, Oklahoma at 00 GMT on May 5th, 2007. The dashed red curve and the light- and dark-blue dots show, respectively, pseudo adiabatic, reversible and entraining plume ascents from 965 hPa (which is near the surface).

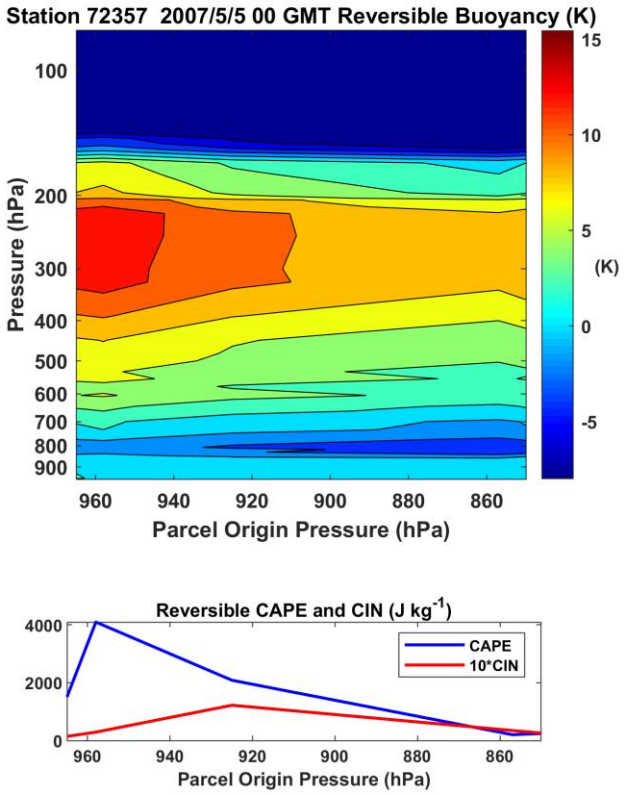

Figure 3.16: As in Figure 3.13, but for Norman, Oklahoma at 00 GMT on May 5th, 2007

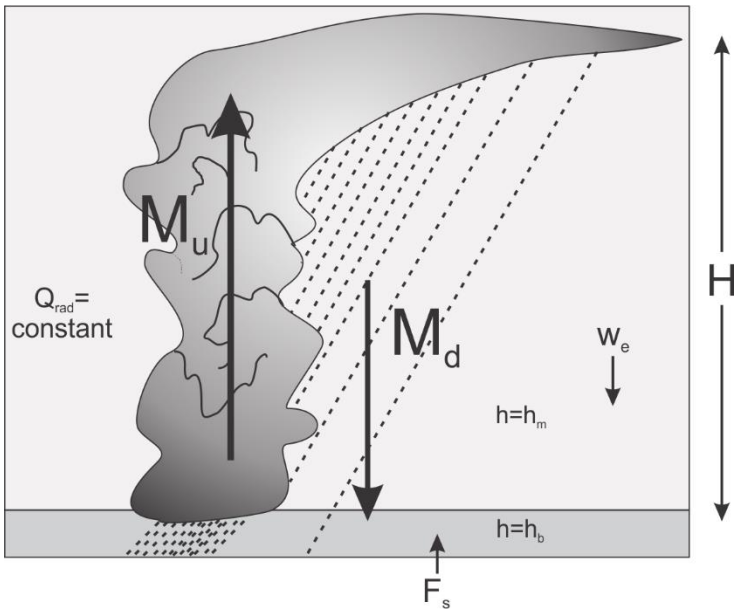

Figure 3.17: Very simple model of moist radiative-convective equilibrium. See text for full description.

We will take the thin subcloud layer to have a moist static energy of h_b and characterize the moist static energy just above the subcloud layer as having the value h_m.

Given the radiative cooling rate Q_{rad} we wish to find the convective mass fluxes and the moist static energies of this very simple system.

We begin with the energy balance of the subcloud layer. The flux of moist static energy from the middle troposphere must balance the flux from the surface:

$$\begin{aligned} F_s &= (M_d + \rho w_e)(h_b - h_m) \\ &= M_u (h_b - h_m), \end{aligned} \tag{3.19}$$

where we have used (3.17) for the second line of (3.19). This can be written alternatively as

$$M_u = \frac{F_s}{h_b - h_m}, \tag{3.20}$$

showing that the convective updraft mass flux increases with increasing surface enthalpy flux and decreasing difference between the moist static energies of the subcloud layer and lower free troposphere.

Next we consider the energy balance in the clear, subsiding air. Here, the radiative cooling must be balanced by the vertical advection of dry static energy, h_d. This may be expressed by

$$\rho w_e \frac{dh_d}{dz} = Q_{rad}. \tag{3.21}$$

Henceforth we will use the symbol S in place of dh_d/dz to denote the dray static stability. As we have seen earlier in this chapter, the virtual temperature lapse rate in the tropics falls nearly along a reversible adiabat, so S is really just a function of the temperature of the system.

Using (3.17) to eliminate w_e gives

$$M_u - M_d = \frac{Q_{rad}}{S}. \tag{3.22}$$

Next we provide a crude representation of the microphysics that drive deep downdrafts by relating the downdraft mass flux to the updraft mass flux via

$$M_d = \left(1-\epsilon_p\right) M_u, \tag{3.23}$$

where ϵ_p is a bulk precipitation efficiency: the fraction of condensed water that ultimately falls to the ground. If that fraction is zero, there can be no net latent heat release and the downdraft mass flux would equal the updraft mass flux, making it impossible to satisfy (3.22). Also, no precipitation reaching the ground implies zero evaporation from the surface, so this is not a viable limit of the system. At the other extreme, a precipitation efficiency of 1 means that no condensed water re-evaporates and so there can be no deep downdraft.

Substitution of (3.23) into (3.22) gives

$$M_u = \frac{Q_{rad}}{\epsilon_p S}. \tag{3.24}$$

Thus for a given cooling rate the convective updraft mass flux increases with increasing radiative cooling, decreasing precipitation efficiency, and decreasing static stability (i.e. decreasing system temperature). Through (3.23), this is also true of the downdraft mass flux.

Comparing (3.24) to (3.20) implies that

$$h_b - h_m = \frac{\epsilon_p S F_s}{Q_{rad}} = \epsilon_p SH, \tag{3.25}$$

where we have made use of (3.18). Thus the decrease of moist static energy from the subcloud layer to the lower free troposphere increases with static stability (i.e. system temperature) and precipitation efficiency.

Since convecting atmospheres have nearly moist adiabatic lapse rates, the saturation moist static energy, h^* above the boundary layer will be nearly equal to the actual moist static energy of the subcloud layer, so we can write (3.25) as

$$h_b - h_m \simeq h^* - h_m = L_v q^* \left(1 - \mathscr{H}\right) = \epsilon_p SH, \tag{3.26}$$

where $q*$ is a characteristic value of saturation specific humidity just above the subcloud layer and $\mathscr{H}$ is the relative humidity of air entering the top of the subcloud layer. Since SH is the difference between the dry static energy along a moist adiabat, going from the lower troposphere to near the tropopause, and since this difference is nearly equal to $L_v q*$, we have that

$$\mathscr{H} \cong 1 - \epsilon_p, \tag{3.27}$$

consistent with what we found in a more detailed analysis of the RCE water budget in Chapter 2 (see, e.g., 2.91). The more efficient the formation and fallout of precipitation, the drier the free troposphere.

Although the details of the vertical profile of humidity in moist RCE depend on many processes, such as entrainment and detrainment, the basic dependence also on cloud microphysics is unequivocal.

We can complete the specification of the system by representing the surface enthalpy flux by a classical aerodynamic surface exchange formulation:

$$F_s = QH = \rho_s C_k |\mathbf{V}_s| \left(h_0 * - h_b\right), \tag{3.28}$$

where ρ_s is the surface air density, C_k is a nondimensional surface exchange coefficient, $|\mathbf{V}_s|$ is a characteristic surface wind speed, and $h_0 *$ is the saturation moist static energy at sea surface temperature. (For the present purpose, we assume that this is a known property of the system). Turning this around, we have

$$h_b = h_0 * - \frac{QH}{\rho_s C_k |\mathbf{V}|}, \tag{3.29}$$

which yields the subcloud layer moist static energy as a function of the sea surface temperature, the integrated radiative cooling of the atmosphere, and the surface wind speed. Note that smaller surface winds result in lower moist static energy of the subcloud layer.

Using (3.29) and (3.25) gives an expression for the moist static energy just above the subcloud layer:

$$h_m = h_0 * - \epsilon_p SH - \frac{QH}{\rho_s C_k |\mathbf{V}|}. \tag{3.30}$$

Thus if we are given the radiative cooling of the troposphere, the surface temperature, and the surface wind speed, along with the precipitation efficiency and the system temperature, we can determine the convective mass fluxes and the moist static energies. Note in particular the important role of surface winds, which in a single-column model must be specified. This is because, except in conditions of very light wind, the surface turbulent flux of enthalpy is largely determined by wind rather than by convective instability. We will return to this important point in Chapter 4.

Simple models like this one serve to illuminate some of the basic elements of moist RCE. For example, in Chapter 4 we will develop a variant of the relationship (3.20) between cloud base

mass flux and surface enthalpy fluxes as a more general way of representing convection in time varying systems with large-scale circulations. But the really interesting physics, largely absent in the case of dry convection, involve the two-way interaction of convection and water vapor (and clouds), wherein the convection controls the water profile which in turn largely determines the radiative cooling profile, which drives the convection. This interaction is sufficiently complex, depending strongly on turbulent and microphysical processes in clouds, that moist RCE is not really very well understood even today.

Superficially, there appear to be some nice parallels with dry convection. We observe that the temperature profile of moist convecting atmospheres lies along a reversible moist adiabat, and we could just adjust steeper profiles back to an adiabat, the way we often handle dry convection.

But which value of reversible entropy should we adjust to? In the dry problem, we insist that energy be conserved, so that the dry static energy of the adjusted state equals that of the initial state. This produces a unique solution. In the moist problem, we must also insist that static energy (moist static energy in this case) be conserved in the adjustment, but we know from observations that the profiles of moist static energy in convecting atmospheres are nowhere near constant in altitude. (A typical profile of moist static energy will look very much like the profile of θ_e, an example of which is shown in Figure 3.12.) Thus we have an integral constraint on the adjusted moist static energy profile but that is not sufficient to tell us what adiabat to adjust to. In moist RCE, the convective effects on temperature and moisture are inextricably bound.

One of earliest attempts to deal with moist convection in moist RCE states was that of Manabe and Strickler (1964), who simply held the specific humidity of the atmosphere to be unaffected by convective adjustment. They merely set any lapse rates in excess of a critical rate of $6.5\,K\,Km^{-1}$ back to the critical rate, holding constant the mass-weighted vertical integral of the dry static energy. Thus there was no feedback of convection to moisture in this early simulation. Three years later, they allowed for a limited feedback by assuming that the relative rather than absolute humidity remains constant (Manabe and Wetherald, 1967).

When general circulation models were first developed, they often suffered from a catastrophic numerical instability that occurred when the model atmosphere became unstable to moist convection. Mostly to avoid this problem, Manabe et al. (1965) developed what amounts to an internal convective adjustment of explicitly simulated clouds for use in general circulation models (GCMs). Whenever the relative humidity equals or exceeds 100% and the lapse rate is steeper than $6.5\,K\,Km^{-1}$, the lapse rate is adjusted back to the critical value assuming that the mass-weighted vertical integral of moist static energy is conserved and that the air remains saturated at all levels adjusted, while any condensed water is immediately removed. The assumption of 100% relative humidity within the region of adjustment suffices to close the problem.

This is a well-defined and unique adjustment, but makes an extreme assumption about condensed water. Consequently, it produces unrealistic profiles of relative humidity, as we will see presently. But it did what it was designed to do, which is to prevent GCMs from blowing up. While the absolute humidity was predicted, it was not used in the radiative transfer calculations

in the GCM simulations described in the 1965 paper, so they could not be said to be two-way interactive.

After the seminal work of Manabe and his colleagues, work on convection focused for some time on the problem of relating the intensity of convection to large-scale variables; this was often referred to as the "closure problem". In the 1960s and 70s, there was a move to relate the intensity of moist convection to the supply of water rather than of energy. Schemes based on the convergence of moisture in the boundary layer enjoyed a brief period of popularity, but suffered from certain pathologies. For example, large quantities of CAPE could accumulate in regions where the imposed criterion of positive moisture convergence was not satisfied. When moisture convergence ensued, CAPE was released suddenly, resulting in a strong positive feedback and grid-scale noise, sometimes referred to as "grid-point storms". The moisture-convergence schemes got into trouble because they largely disregarded the simple fact that convection is driven by thermal instability.

The central role of energy in controlling convection was re-affirmed by the "quasi-equilibrium" hypothesis introduced by Arakawa and Schubert (1974). This hypothesis holds that convection consumes available potential energy at the rate that it is supplied by larger-scale processes such as surface fluxes and radiative cooling, much as the rate of boiling in a pot of water is controlled by the heat input from the stove, rather than the temperature of the water, once the latter is at the boiling point.

The work of Arakawa and Schubert (1974) inaugurated a period of a few decades in which representations of moist convection were either built explicitly on the quasi-equilibrium hypothesis or implicitly, by assuming that convection restores thermal stability or neutrality on short time scales. This allowed researchers to focus their attention on the much more challenging problem of convective control of moisture.

As we have seen earlier in this chapter, moist convection keeps the temperature profile close to a suitably defined adiabat, but there is no simple constraint on the shape of the water profile. Moreover, it takes substantially longer for the moisture field to return to its RCE profile after being perturbed than it does the virtual temperature field. In essence, the adjustment time for virtual temperature is dictated by the time it takes deep internal buoyancy waves to travel between clouds (Bretherton and Smolarkiewicz, 1989). A typical phase speed of a mode whose vertical half-wavelength spans the troposphere is around $35\,ms^{-1}$, and if the cloud spacing is around $100\,km$, this gives an adjustment time on the order of an hour. But moisture responds on a much longer time scale…basically, the time it takes for turbulent diffusion to spread moisture anomalies from clouds to their environment; internal waves act to eliminate buoyancy perturbations, not perturbations of passive tracers.

We can estimate a time scale for moisture adjustment by writing a budget equation for the moist static energy, h_e, of air in between deep convective clouds:

$$\frac{\partial h_e}{\partial t} = -w_e \frac{\partial h_e}{\partial z} + \frac{Q_{rad}}{\rho} - \nabla \bullet \mathbf{V}' h_e', \tag{3.31}$$

where w_e is the vertical velocity in the clear air, Q_{rad} is the radiative heating rate, and the last term in (3.13) represents the eddy diffusion of moist static energy. To get a time scale, we will

look at a level in the atmosphere at which h_e has its minimum value, so that that the first term on the right of (3.13) is small there. We will suppose that variations in the radiative cooling rate are of secondary importance in setting the adjustment time scale. Finally, we will suppose that the fluctuating part of the moist static energy scales as the difference between the cloud moist static energy, h^*, and the clear air value, while a characteristic inter-cloud spacing is denoted by L. Thus, from a scaling point of view, we have, from (3.31)

$$\frac{h_e'}{\tau_m} \sim \frac{V}{L}\left(h^{*\prime} - h_e'\right), \tag{3.32}$$

where V is a characteristic horizontal velocity in between clouds and τ_m is the moisture adjustment time scale we seek. From mass continuity in the air in between clouds,

$$\frac{V}{L} \sim \frac{w_e}{H},$$

where H is roughly half the depth of the troposphere. From this and (3.32),

$$\tau_m \sim \frac{H}{w_e}, \tag{3.33}$$

that is, the characteristic time scale for moisture adjustment is the time it takes air subsiding in between clouds to traverse half the troposphere. If we use (3.21) for the vertical velocity scale in the clear air, we get

$$\tau_m \sim \frac{\frac{\partial h_d}{\partial z} H \rho}{Q_{rad}} \sim \frac{L_v q^* \rho}{Q_{rad}}, \tag{3.34}$$

where in the second part we have made use of the fact that the total change in dry static energy along a moist adiabat is roughly equal to $L_v q^*$, where q^* is a characteristic value of the saturation mixing ratio in the lower troposphere. This shows that the adjustment time increases with temperature, since q^* varies according to Clausius-Clapeyron, while Q_{rad} increases somewhat more slowly with temperature.

If we use typical tropical values for the quantities in (3.34) ($q^* \simeq 0.02$ and a radiative cooling rate of $1\,K\,day^{-1}$) this time scale is around 35 days, about 400 times longer than the virtual temperature adjustment time scale. Later in this chapter, we will see that these numbers are consistent with those characterizing adjustment to equilibrium in a fairly comprehensive single-column model. In particular, the moisture time scale, as it is longer, is the rate-limiting factor in adjusting to RCE in systems in which the surface temperature is specified.

The great disparity between the buoyancy and moisture adjustment time scales has profound consequences for tropical dynamics and for practical aspects of representing moist convection in models. Moist importantly, some of the errors in the representation of convection may not be apparent on time scales much shorter than the moisture adjustment time, so that tests of convective schemes against observations require long time series of the latter.

Moist convective adjustment is fundamentally nonlocal. That is, introducing a perturbation to RCE at some particular level does not usually result in a relaxation at that level alone. For example, suppose a positive temperature perturbation is applied to the RCE state at some instant in time. If it is large enough, convection will be temporarily prevented from reaching levels above that level, so that the convective heating will be temporarily shut down not just at the level in which the temperature perturbation was introduced, but all levels above that. Moreover, if this affects moist convective downdrafts, levels below the perturbation level will also be affected. The adjustment cannot be represented as a simple relaxation back to the RCE profile.

For virtual temperature, this may not matter much in practice because the total adjustment is fast and, integrated over the whole period of relaxation, the effect is simply to damp the original perturbation.

But for moisture, the non-locality of the adjustment may have repercussions over a significant period of time, affecting the evolution of the system on time scales that are not short compared to, e.g., atmospheric circulation systems.

For this reason, representations of moist convection that simply relax temperature and moisture profiles back to empirical equilibrium profiles have largely been abandoned in favor of approaches in which bulk measures of convective activity are based either explicitly on the quasi-equilibrium hypothesis, as in the original work of Arakawa and Schubert (1974) and its successors, or implicitly as in so-called “CAPE-based” mass flux schemes. In such schemes, convective mass fluxes are formulated so as to consume available potential energy quite rapidly (but not usually instantaneously), keeping CAPE from building up and thereby effectively, if somewhat gently, enforcing quasi-equilibrium. But the convective mass fluxes are then coupled with representations of cloud physical and turbulent processes to calculate water fluxes by the convection, and these are then used to calculate convective tendencies of water at each model level. In RCE, these tendencies will necessarily be zero above the subcloud layer, since there are no non-convective sources of water in the cloud-bearing layer.

Reasonably formulated mass-flux convective schemes keep the tropical temperature lapse rate near some moist adiabat or a profile based on neutrality to an entraining plume. But the convective moistening profile inevitably depends on myriad assumptions about how entrainment and cloud physics operate in clouds (and, indeed, how these to processes interact), so that a typical convective scheme has many parameters very few of which, if any, can lay any claim to universality. Moist convective schemes are Gothic affairs and it is hardly surprising that they are usually the first sub-grid scale representations to be blamed for what goes wrong with models, or that the community as a whole is trying to get away from them by explicitly simulating at least deep moist convective clouds, even in climate models. Yet the some of the basic challenges remain with explicit convection including how to deal with the all-important (and usually sub-grid-scale) turbulence and associated entrainment and how to represent cloud microphysical processes, which will always be unresolved. A somewhat less explored issue is how deep moist convection controls stratiform clouds such as cirrus anvils and boundary layer clouds, all of which have strong influences on radiative transfer.

Among the many challenges of representing moist convection in models is dealing with clouds and water vapor in the upper troposphere. In the high portion of deep convective clouds, the condensed water content exceeds the saturation vapor content, often by a large factor, yet not

all convective schemes detrain condensed water into the environment, and very few pay much attention to making good estimates of the amount of ice water in the tops of deep cumulonimbi. Although the absolute water vapor content of the upper troposphere is small, it is nonetheless a very important absorber and emitter of radiation, as are high clouds, which also can have large albedos. We will see later in this chapter that high clouds are important in the phenomenon of self-aggregation of deep convection, so that getting them wrong may have serious consequences for weather and climate. In particular, the interaction of convectively produced high clouds with radiation is a key factor in low frequency variability in the equatorial region and in the genesis and intensification of tropical cyclones.

Owing to the large number of ad-hoc parameters it is vital to test them against observations. These tests can also help calibrate the parameters. One way to do this is to carry out field experiments designed to collect enough data over a sufficient period of time to supply a single-column model with everything it needs, except for convection, to predict the evolution of the vertical profile of humidity over time. This, of course, is much easier to say than to do.

Consider first the budget equation for the conservation of moist static energy, h, excluding a term proportional to the time dependence of the pressure field:

$$\frac{\partial}{\partial t}(\rho h) + \nabla\bullet(\rho \mathbf{V} h) = -\frac{\partial F_r}{\partial z} - \frac{\partial F_t}{\partial z}, \tag{3.35}$$

where $\mathbf{V}$ is the three-dimensional velocity vector, F_r is the radiative energy flux, and F_t is the total turbulent enthalpy flux, including that by moist and dry convection. These two fluxes are approximated as being purely in the vertical. To test the ability of a representation of moist convection to predict the evolution of the moist static energy, it is necessary to measure that evolution together with horizontal and vertical advection of moist static energy, radiative fluxes, and turbulent fluxes in the subcloud layer, including from the surface. And these must be done over periods of at least tens of days to capture the evolution time scales of moist static energy.

Making these measurements is quite challenging. Estimating the small but critically important vertical velocity is especially difficult. One strategy is to carefully measure horizontal velocities over a closed circle or polygon and use mass continuity to estimate the vertical velocity. One example of an effort to do this occurred during a field experiment, the Tropical Ocean Global Atmosphere (TOGA) Coupled Ocean Atmosphere Response Experiment (COARE), conducted in 1992-1993 in the tropical South Pacific. Figure 3.18 shows a polygon of 4 vertices at which rawinsondes were launched at 6-hour intervals.

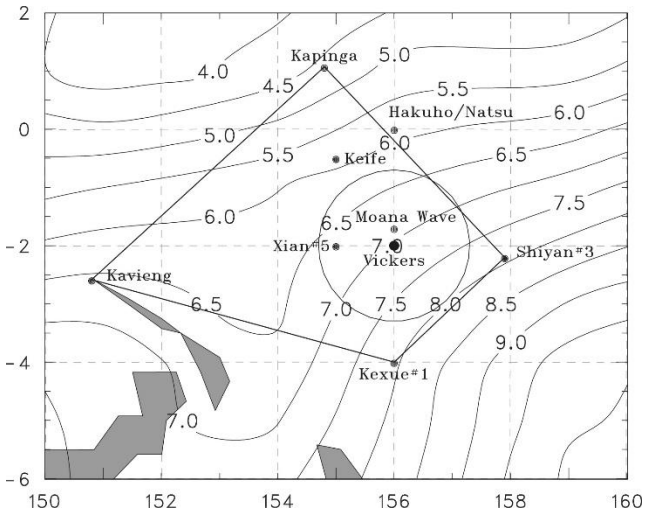

Figure 3.18: TOGA COARE Intensive Flux Array (IFA), which operated from November 1st 1992 to February 28th 1993. The contours are of mean rainfall (mm day-1) over the 4-month period.

Unfortunately, there are several gaps in soundings from the two southeastern-most stations. In the end, estimating vertical velocity from mass continuity applied to horizontal wind and density estimates at only 4 stations is prone to sampling and instrumental errors.

In addition to rawinsonde measurements of temperature, moisture and horizontal winds, radiometers on moored buoys measured surface radiative fluxes, and top-of-the-atmosphere radiative fluxes were measured by satellites. These radiometric measurements do not capture the vertical structure of the radiative fluxes, and either an assumption must be made about their vertical structure, or radiative fluxes must be calculated from a radiative code. Surface sensible and latent heat fluxes were measured from moored buoys.

The lack of energetic consistency of the measurements can be demonstrated by integrating (3.35) through the depth of the troposphere, assuming that vertical velocity vanishes at the tropopause and using mass continuity:

$$\frac{\partial}{\partial t}\left(\rho h\right) + \rho \mathbf{V}_2 \bullet \nabla h + \rho w \frac{\partial h}{\partial z} = F_{R0} - F_{TOA} + F_s, \tag{3.36}$$

where the symbol $\sim$ indicates a vertically integrated quantity, F_{R0} and F_{TOA} are the net upward radiative fluxes at the surface and top-of-the-atmosphere, respectively, and F_s is the turbulent flux of enthalpy from the surface. There is no contribution to (3.36) from moist convection because convection cannot change the column mean enthalpy, it can only redistribute it in the vertical.

We can now integrate (3.36) in time using observational estimates of the horizontal and vertical advections, radiative fluxes, and surface enthalpy fluxes. When this is done for the whole 4-month period of the TOGA COARE IFA measurements, the predicted value of the vertically averaged enthalpy drifts away from its observed value, with an accumulated error at the end of the period amounting to the equivalent of 25 K if that enthalpy error were owing to temperature only (Emanuel and Živkovic-Rothman, 1999). This is a spectacular error and must be accounted for before using the measurements to test the ability of the convection scheme to predict the time evolution of temperature and moisture. Given estimates of the magnitudes of likely errors in

vertical velocities and other quantities in (3.36), a variational approach can be developed to optimally correct for the errors (Zhang and Lin, 1997).

Integrating the moist static energy equation (3.35) for many weeks using a suitably adjusted set of measurements of the advective, radiative and surface flux terms and a convective representation for the last term in the equation provides a fairly rigorous test of the ability of the scheme to predict the evolution of moist static energy. It is an easy test to fail. Since almost all variations of moist static energy above the boundary layer in the tropics are due to variations of moisture, this effectively tests the scheme's ability to simulate vertical moisture fluxes. The scheme must also be able to predict the evolution of the temperature field, though this is much more difficult to evaluate as instrumental and sampling errors of temperature are comparable to typical real temperature variations.

Ideally, a scheme should be able to pass similar tests forced by field measurements in very different meteorological conditions, but not many such field measurements exist. Obtaining the field measurements and then optimizing and evaluating convection schemes against such measurements is arduous and time-consuming. For this reason, not many convective schemes have been rigorously tested against field measurements and instead are optimized to improve the performance of the numerical weather prediction and/or climate models in which they are embedded. But this is problematic, as the optimization may result in a partial compensation for other model errors.

In this text we will use the representation of convection by Emanuel and Živkovic-Rothman (1999). This scheme regulates the flux of mass though cloud base according to the buoyancy of air lifted reversibly and adiabatically from the subcloud layer to the first model level above the lifted condensation level. More buoyancy yields a greater mass flux, resulting in faster stabilization of the atmosphere. The effect is to drive convection toward a form of energy quasi-equilibrium, where convection removes available potential energy at about the rate it is generated by larger-scale processes such as radiative cooling and surface enthalpy fluxes.

The mass ascending through cloud base in then partitioned into a number of branches that may be as large as the number of model levels between cloud base and cloud top. Air in each branch first ascends reversibly and adiabatically to a particular model level, where a fraction of the condensed water is removed. This fraction depends on the water content itself as well as temperature. Once the condensed cloud water has been adjusted, the sample mixes with the unperturbed environment, resulting in an integer number of samples of varying fractions of environmental air mixed in. Each mixture then ascends or descends, reversibly and adiabatically, to its level of neutral buoyancy, where it is detrained into the environment.

The removed condensate is added to a single, unsaturated downdraft driven by evaporation of the falling condensate; this unsaturated downdraft transports energy and water and can affect the thermal properties of the subcloud layer.

The convection scheme is also coupled to a representation of stratiform clouds, such as anvil clouds, that are a direct result of moist convection in the atmosphere (Bony and Emanuel, 2001). Downdrafts produced by the scheme also alter surface fluxes primarily by changing the mean wind speed at the surface.

The free parameters of the scheme include the specification of the fractions of condensed water converted to precipitation as functions of temperature and water content, the rate of fall and re-

evaporation of precipitation, and the fraction of precipitation that falls though environmental air, as opposed to cloud. All of these parameters affect the behavior of the scheme and the evolution of atmospheric water vapor in models that employ the scheme. The values of the parameters have been adjusted to optimize the evolution of the vertical profile of relative humidity in a single-column model driven by TOGA-COARE IFA data, as described earlier in this section.

To provide a relatively straightforward simulation of moist RCE, we design a "single-column model" (sometimes referred to as an "SCM") that consists of the aforementioned convection scheme coupled to the radiative transfer scheme of Morcrette (1991). The radiative transfer scheme is able to handle clouds and aerosols, and the cloud properties are represented according to Bony and Emanuel (2001). Concentrations of the important long-lived greenhouse gases and aerosols are prescribed as constants or as functions of height, but clouds and water vapor are calculated interactively. Dry convection is represented by a simple dry-adiabatic adjustment, and conserved tracers and water concentration are made uniform with height by any such adjustments. If water condenses explicitly during the adjustment, the condensed water is assumed to precipitate with no re-evaporation. Surface fluxes are calculated using simple aerodynamic flux formulae, with a background wind supplied as an external parameter, augmented by downdrafts produced by the moist convection scheme.

Finally, the surface itself is represented as a single slab of water, although the evaporation rate can be artificially altered to loosely simulate land surfaces with restricted water availability. The slab's temperature can be either specified or calculated from surface energy balance.

The SCM is integrated forward in time starting from a specified sounding whose vertical structure also specifies the vertical structure of the SCM. Although the model rarely achieves a strictly time-independent state, it does eventually come into a state of statistical equilibrium in which there are no trends in the thermodynamic properties of the system.

The SCM described here can be run on ordinary laptop or desktop computers and is **available through the website for this book**.

The final RCE state is not steady but rather fluctuates around a stable equilibrium state, with near balances between precipitation and surface evaporation, and between incoming solar and outgoing longwave radiation.

The temperature profile of the equilibrium state is compared to that of pure radiative equilibrium and radiative-dry-convective equilibrium in Figure 3.19. Note that the moist RCE solution is very close to an average observed vertical profile of temperature in the tropics, except in the lower stratosphere. In this case, the surface air temperature is only a few degrees cooler than the sea surface temperature, but the relative humidity of near surface air is only around 80%, so there is still a profound thermodynamic disequilibrium between the sea and the air, but it shows up mostly in the latent heat term.

The state shown in Figure 3.19 is still not a fully interactive calculation as the relative humidity has been fixed at an observed profile. Figure 3.20 shows the relative humidity in a fully interactive calculation, in which the precipitation efficiencies are dependent on condensed water content and temperature. This is compared to the humidity profile of three other simulations, in which the surface temperature has been fixed at the control value but the precipitation

efficiencies have been set to either 0.1 or 1.0 everywhere, and in the last case the evaporation of precipitation has been turned off.

In the control experiment, the precipitation efficiencies and other parameters have been set so as to optimize a comparison between predicted and observed relative humidity, as a function of altitude, during the 4 months of TOGA COARE IFA measurements (Emanuel and Živkovic-Rothman, 1999). When the precipitation efficiency is set to 0.1 everywhere, the entire upper troposphere becomes saturated owing to the high condensed water content of air detrained from deep convective clouds. The lower troposphere actually becomes drier than the control, at least in part because the control precipitation efficiencies are less than 0.1 there. Thus there is more condensed water detrained from shallow clouds in the control experiment.

When, on the other hand, the precipitation efficiencies are set to 1 everywhere, the whole troposphere becomes substantially drier, except in a thin layer just above the subcloud layer. When in addition, the evaporation of precipitation is turned off a dry limit is reached that is determined by the balance between drying by subsidence between clouds and detrainment of just-saturated air from the clouds.

While the imposed changes in precipitation efficiencies here are deliberately extreme, they illustrate that the humidity of the atmosphere in RCE is sensitive to cloud microphysical processes.

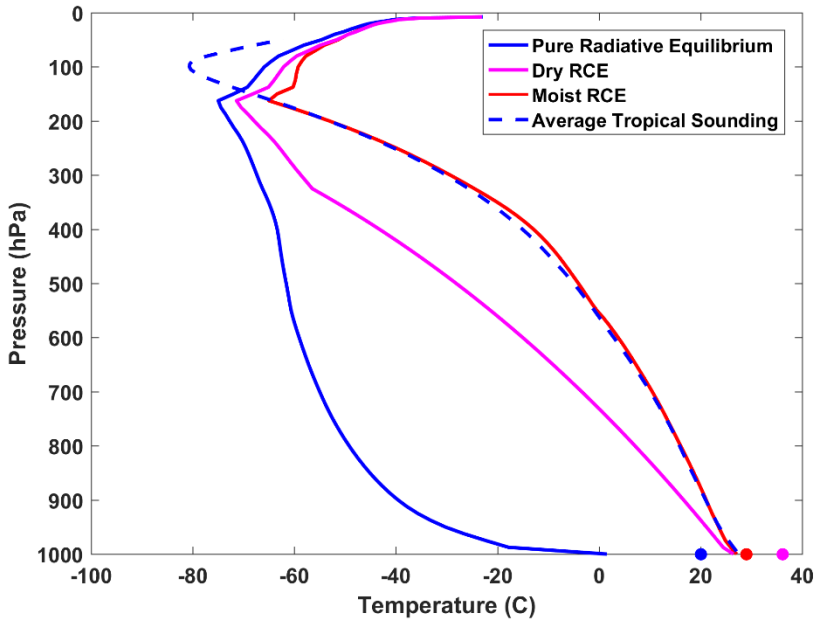

Figure 3.19: As in Figure 2.14 but also showing a fixed relative humidity, moist RCE solution from the single-column model in red.

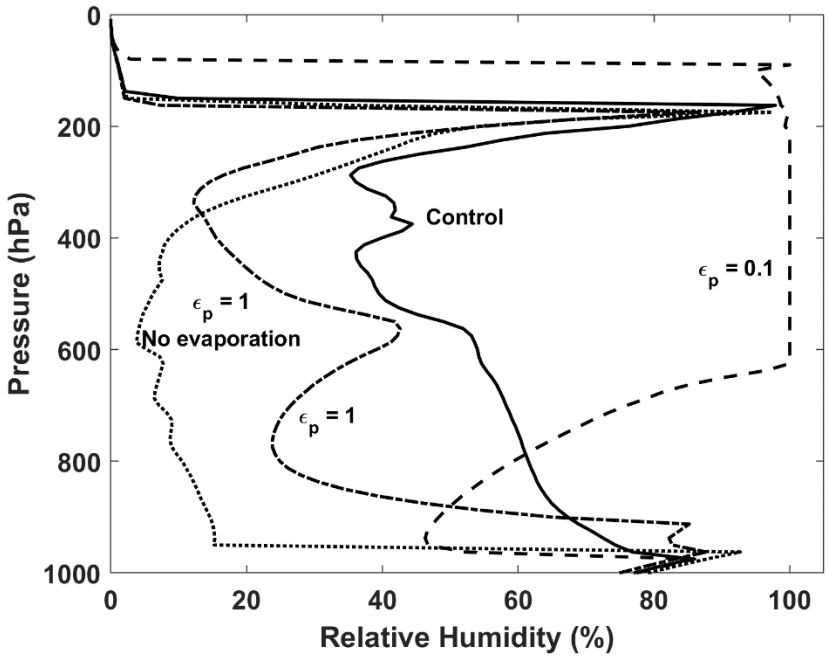

Figure 3.20: Profiles of relative humidity (%) in moist RCE for the standard formulation of parcel precipitation efficiencies (solid), for $\epsilon_p = 0.1$ *(dashed),* $\epsilon_p = 1$ *(dash-dot), and* $\epsilon_p = 1$ *with no evaporation of precipitation (dotted).*

Table 1 shows the external conditions for the control experiment, driven by annual average solar radiation, and omits all clouds, while Table 2 lists values of the some of the important parameters averaged over the last 100 days of the experiment.

Table 1: Control run conditions

Latitude (degrees)	Surface albedo	Mean Surface Wind Speed (m/s)	CO_2 (ppm)	CH_4 (ppm)	N_2O (ppb)	CFC-11 (ppt)	CFC-12 (ppt)
23.0	0.248	5.0	360.0	1.72	310.0	280.0	484.0

Table 2: Value of key time-averaged quantities, control run

Surface T (C)	Precipitation (mm/day)	Evaporation (mm/day)	TOA net shortwave (W/m^2)	TOA net longwave (W/m^2)	Surface net shortwave (W/m^2)	Surface net longwave (W/m^2)	Net surface radiative (W/m^2)	Surface sensible (W/m^2)	Surface latent (W/m^2)	Net surface turbulent flux (W/m^2)
27.0	4.215	4.222	-296.71	296.89	-217.13	85.10	**-132.03**	10.81	121.46	**132.27**

Note the near balances between surface evaporation and precipitation, top-of-the-atmosphere (TOA) net shortwave (incoming minus reflected shortwave) and outgoing longwave radiation, and net surface radiative and turbulent fluxes. In principle, there should be exact balances, but this is almost never seen in models because of both physical and numerical errors in the computations. For example, heating by the frictional dissipation of falling precipitation in the model amounts to about $1.4\,Wm^2$, almost an order-of-magnitude greater than the energy imbalance at the top of the atmosphere. Thus omitting this seemingly insignificant energy conversion would greatly increase the magnitude of the TOA energy imbalance. Similarly, cooling of the air by precipitation falling through a temperature gradient cools the system by around $0.6\,Wm^2$. The convection scheme internally advects air upward and downward, and while real advection is thermodynamically reversible, finite difference schemes may not exactly conserve both energy and entropy, so some of the excess upward longwave radiation at the top of the atmosphere may be owing to numerical generation of entropy in the convection scheme. Getting near balance in TOA radiation requires great attention to apparently small thermodynamic details.

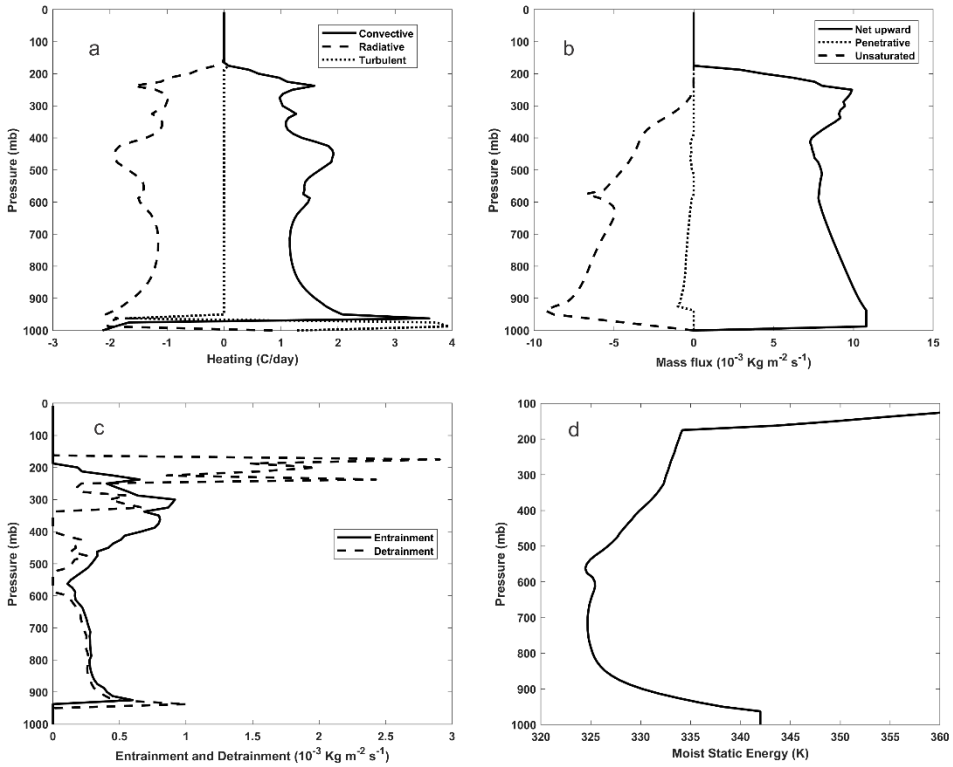

Figure 3.21: Vertical profiles of control moist radiative-convective equilibrium solution. a) Heating rates (expressed in K day^{-1}): Net convective (solid), radiative (dashed) and boundary layer convective adjustment (dotted); b) Convective mass fluxes: Upward (solid), saturated in-cloud downdrafts (dotted) and unsaturated downdrafts driven by evaporation of precipitation (dashed); c) Convective entrainment (solid) and detrainment (dashed); and d) moist static energy (divided by heat capacity). These profiles have been averaged over the last 10 days of the simulation.

Vertical profiles of various quantities, averaged over the final 10 days of the control simulations, are shown in Fig. 3.21. Convection heats the troposphere at about 1.5 K day^{-1}, with only fairly

weak variations with height, and radiation cools the atmosphere at the same rate. In the subcloud layer, dry convection heats the boundary layer at about 3.5 K day-1, compensating both radiative cooling and cooling by evaporation of rain, the latter of which is included in the definition of convective heating. Fig. 3.21 b shows the vertical profiles of convective mass fluxes, partitioned into updrafts, saturated downdrafts driven by the evaporation of cloud water, and unsaturated downdrafts driven by the evaporation of falling precipitation. Saturated downdrafts play a minor role in RCE but, as we shall see in the next chapter, are very important in shallow convective boundary layers.

The convection scheme used here has a spectrum of updrafts and downdrafts, so the net mass entrainment/detrainment is not a simple vertical derivative of the net mass fluxes. For example, air at some level may both detrain from a shallow cloud and be entrained into a deep cloud. The profiles of entrainment and detrainment for this RCE state are shown in Figure 3.21c. Note that profiles of both are quite similar below 600 hPa, but diverge above that level, with strong detrainment near the tropopause, as one would expect.

The equilibrium moist static energy profile (Fig 3.21d) shows a broad minimum in the middle troposphere and a well-mixed subcloud layer. The profile is qualitatively very similar to that of equivalent potential temperature (θ_e) seen in tropical soundings (e.g. Fig. 3.12). Convection mixes high moist static energy air in the subcloud layer into the free troposphere, coupling the strong surface source with the deep troposphere, while radiative cooling provides the balancing sink.

b. Behavior of global perturbations to RCE

The statistical equilibrium state of moist RCE is a useful zero-order approximation to the actual state of the tropical atmosphere, and thus a good starting point for understanding the meteorology of the tropics. Naturally, the real atmosphere is evolving in time and there can be substantial flows of energy by large-scale circulations, pushing the state away from RCE. As a first step to understanding the effects of time dependence and horizontal flows of energy and water, we can ask how the RCE state responds to global (that is, horizontally homogeneous) perturbations in the boundary and/or initial conditions, focusing on the characteristic time scales and structural aspects of the response.

In essence, we can characterize the response by three time scales: The time it takes for the troposphere to relax back to RCE holding the surface temperature fixed, the time it takes the surface to relax back to RCE holding the whole atmosphere fixed, and the relaxation time scale for the coupled system. This last is a function of the first two time scales, but defies intuition in being much longer than either the ocean-only or atmosphere-only time scales.

We begin by performing some simple experiments with the single-column model described earlier in this chapter. These experiments all begin with a moist RCE state achieved by running the model into equilibrium with a slab ocean surface whose temperature is calculated from surface energy balance. In the first experiment, we fix the surface temperature and subtract 3 K from all the air temperatures below the 100 hPa level, then run the model until equilibrium is regained.

As can be seen in Fig. 3.22, the recovery of precipitation and temperature in the troposphere has a time scale of around 10 days. Above the RCE tropopause, located near the 175 hPa level, the relaxation time scale is somewhat longer. Note that the relaxation cannot be described as a smooth exponential. This may be partially owing to the nonlinearities of radiative and convective transfer and also to the particular way the convection scheme is designed.

Fig. 3.23 shows the results of holding atmospheric temperature and water vapor fixed at their RCE profiles and perturbing the initial sea temperature by -3 K. In this case, the surface is a 1m thick slab of water. Recovery to RCE is smooth and rapid, occurring with a relaxation time scale of around 1-2 days. Here it should be noted that the recovery time is proportional to the thickness of the slab of water. Thus the recovery of a 50 m slab, more representative of the ocean's surface mixed layer, would have a relaxation time scale of around 50-100 days.

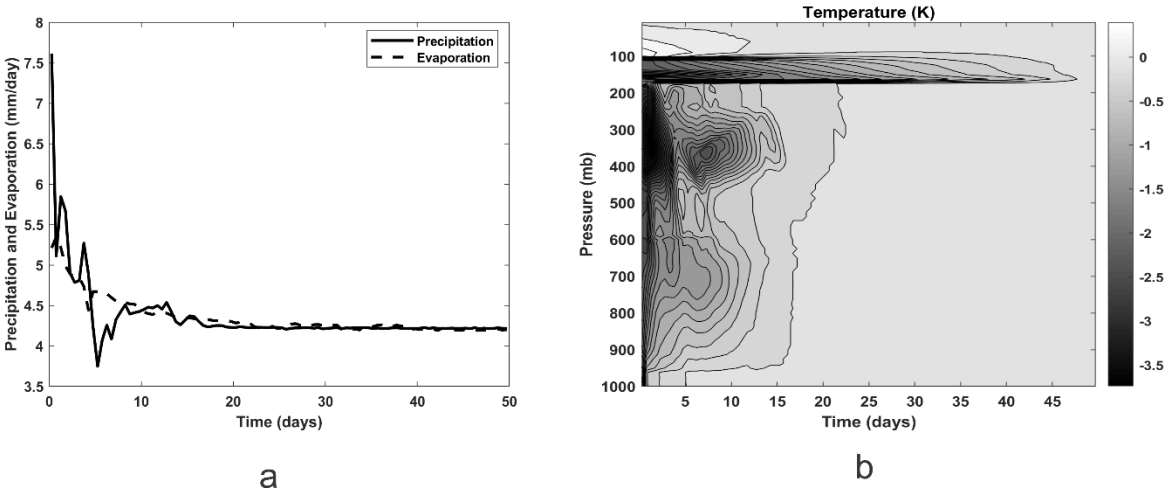

Figure 3.22: Recovery from 3K cooling below 100 hPa to a moist RCE state. The surface temperature is fixed at its RCE value. a) Surface precipitation (solid) and evaporation (dashed), in mm/day. b) Departure of temperature (K) from RCE.

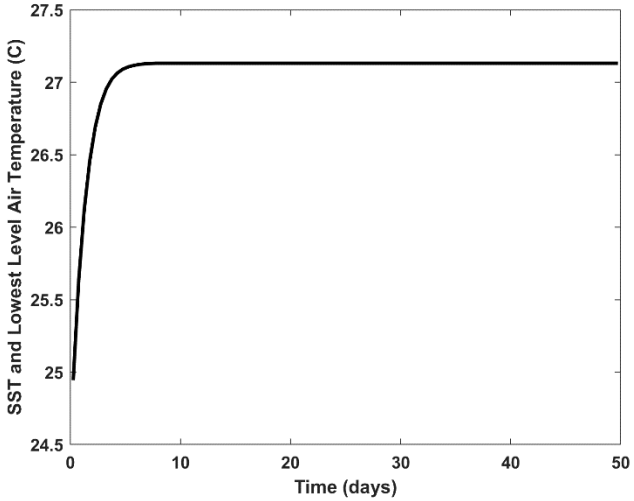

Figure 3.23: Recovery of a 1m thick ocean slab to RCE from an initial -3 K anomaly. In this experiment, the properties of the atmosphere are held constant at their RCE values.

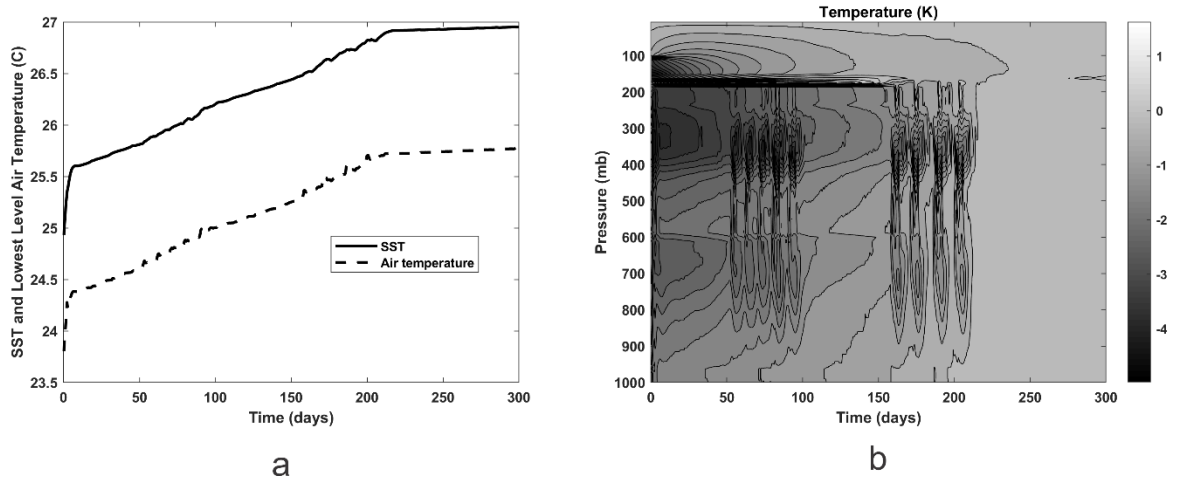

Figure 3.24: Recovery of the coupled ocean-atmosphere system to RCE from a -3K perturbation to the atmosphere below the 100 hPa level and a -2 K perturbation to the temperature of a 1m thick slab of water. a) Water temperature (solid) and surface air temperature (dashed), in C. b) Time-pressure section of the perturbation of temperature (K) from the RCE state.

The relaxation of the coupled system back to RCE is shown in Fig 3.24. The time scale of the relaxation is around 200 days, *much* longer than either the atmospheric relaxation time of 10 days or the ocean time of 5 days.

Why is the coupled time scale so much longer than either of the uncoupled scales? To see this, we will construct a very simple model of the coupled system, illustrated in Figure 3.25 (Cronin and Emanuel 2013). A troposphere with a uniform value of saturation most static energy, h^*, overlies a slab of water of depth Δz_{ml} and a turbulent enthalpy flux F_c transports energy from the ocean to the atmosphere. At the top of the atmosphere the longwave radiative flux is F_{rad}. The following simplifying assumptions are made to obtain analytic solutions:

- The lower troposphere is virtually opaque to infrared radiation, so that all the energy flux from the water to the air is carried by turbulence.
- The relative humidity profile of the atmosphere is fixed, so that changes in the radiative flux may be expressed in terms of changes in $h*$ alone.
- Changes in the absorption of solar radiation by the atmosphere may be ignored.

With these three assumptions, we may write down simple equations for the time evolution of fluctuations in atmospheric temperature, as represented by $h*$ and water temperature, as represented by h_0*:

$$\frac{\Delta p}{g}\frac{dh*'}{dt} = -\frac{dF_{rad}}{dh*}h*' + F_c', \tag{3.37}$$

$$c_l \rho_l \Delta z_{ML} \frac{dT_s}{dh_0*}\frac{dh_0*'}{dt} = -F_c'. \tag{3.38}$$

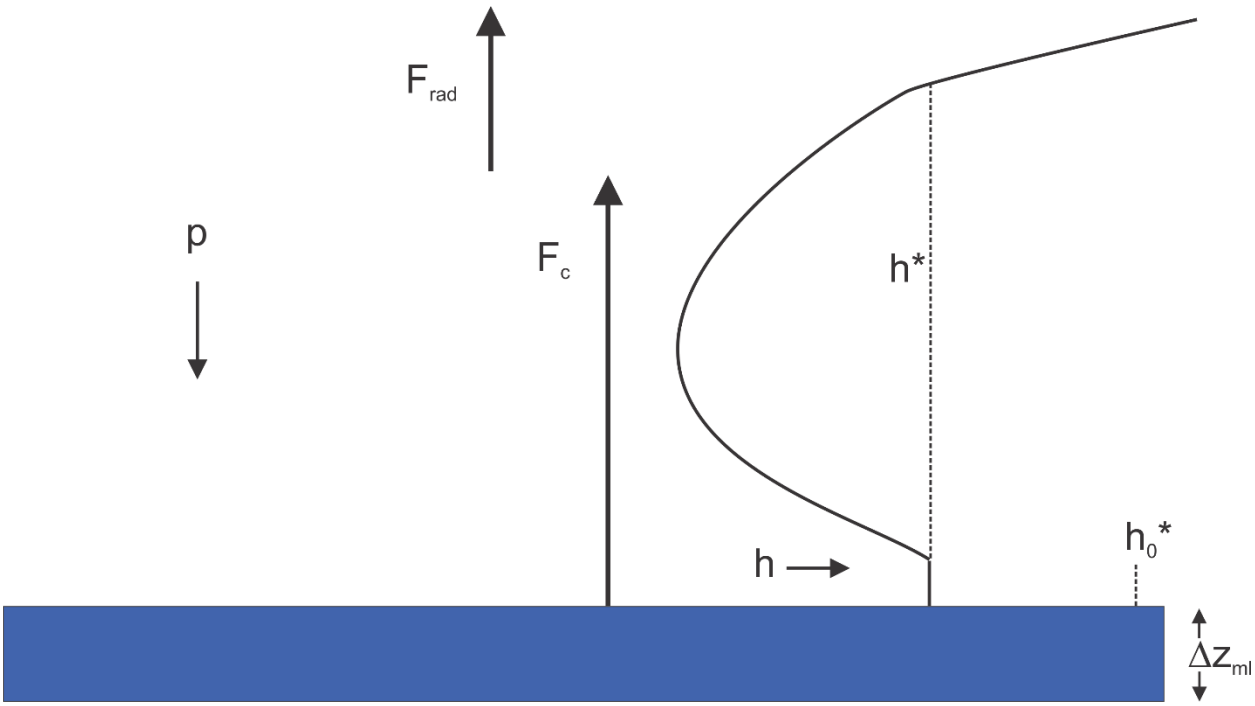

Figure 3.25: Simple model of the coupled system. A troposphere with a moist adiabatic lapse rates rests on a slab of water of uniform temperature and depth Δz_{ml}. The saturation moist static energy corresponding to the water temperature is h_0*. The temperature of the troposphere is characterized by a vertically uniform saturation moist static energy $h*$. The turbulent flux of enthalpy from the water to the atmosphere is F_c and the outgoing longwave radiative flux is F_{rad}.

Here Δp is the pressure depth of the troposphere, g is the acceleration of gravity, and c_l and ρ are the heat capacity and density of liquid water.

Next we represent the surface turbulent enthalpy flux by a classical aerodynamic flux formula:

$$F_c' = \rho_s C_k |\mathbf{V}_s| \left(h_0^{*\prime} - h^{*\prime} \right), \tag{3.39}$$

where ρ_s is the surface air density, C_k is the dimensionless coefficient of enthalpy exchange, and $|\mathbf{V}_s|$ is the surface wind speed, which must be externally specified here as in the single column model. In the last term in (3.39) we have replaced the boundary layer moist static energy by h^* as the two are equivalent of the atmosphere is neutral to moist convection.

The coefficient $\frac{dF_{rad}}{dh^*}$ that appears in (3.37) may be expressed in terms of the traditional climate sensitivity parameter $\lambda \equiv \frac{\partial T_s}{\partial F_{rad}}$, where T_s is the surface air temperature:

$$\frac{dF_{rad}}{dh^*} = \frac{dT_s}{dh^*} \lambda^{-1}. \tag{3.40}$$

The coefficient $\frac{dT_s}{dh_0^*}$ that appears in (3.38) may be derived from the definition of h^* and the Clausius-Clapeyron equation:

$$\frac{dT_s}{dh_0^*} = \left(c_p + \frac{L_v^2 q_s^*}{R_v T_s^2} \right)^{-1} \tag{3.41}$$

We also use this expression for $\frac{dT_s}{dh^*}$ that appears in (3.40) since the surface air and water temperatures are very close to each other in the tropics.

Using (3.39) - (3.41) allows us to express (3.37)-(3.38) as

$$\tau_a \frac{dh^{*\prime}}{dt} = \chi h_0^{*\prime} - h^{*\prime}, \tag{3.42}$$

and

$$\tau_o \frac{dh_o^{*\prime}}{dt} = h^{*\prime} - h_o^{*\prime}, \tag{3.43}$$

where τ_a and τ_o are atmospheric and ocean relaxation time scales given by

$$\tau_a \equiv \frac{\Delta p}{g} \left(c_p + \frac{L_v^2 q_s^*}{R_v T_s^2} \right) \frac{\lambda}{1 + \lambda c}, \tag{3.44}$$

and

$$\tau_o \equiv \frac{c_l \rho_l \Delta z_{ml}}{c}, \tag{3.45}$$

with

$$c \equiv \rho_s C_k \,|\, \mathbf{V}_s \,|\left(c_p + \frac{L_v^2 q_s^*}{R_v T_s^2} \right), \tag{3.46}$$

and

$$\chi \equiv \frac{\lambda c}{1+\lambda c}. \tag{3.47}$$

The form of equations (3.42) and (3.43) makes it clear that τ_a governs the rate at which the atmosphere relaxes to a fixed ocean, while τ_o governs the rate at which the ocean relaxes to a fixed atmosphere. These equations admit exponentially decaying solutions of the form $e^{-t/\tau}$, where

$$\tau = \frac{2\tau_o}{1+\tau_o/\tau_a \pm \sqrt{\left(1+\tau_o/\tau_a\right)^2 - 4\left(1-\chi\right)\tau_o/\tau_a}}. \tag{3.48}$$

Clearly, the longer time scale will be associated with taking the negative root in the denominator of (3.48). From (3.47), if $\lambda c >> 1$, then the last term in the denominator of (3.48) will be relatively small compared to the first term in the discriminant and we can approximate (3.48) as

$$\tau \cong \frac{\tau_a + \tau_o}{1-\chi} = \left(\tau_a + \tau_o\right)\left(1+\lambda c\right). \tag{3.49}$$

Thus, if $\lambda c >> 1$, the coupled time scale given by (3.49) will be large compared to the sum of the time scales of the two individual components of the system.

For example, for an RCE ocean temperature of 27º C, a surface wind speed of $5\, ms^{-1}$, a tropospheric pressure depth of 800 hPa, a water depth of 1 m, and a climate sensitivity (λ) of $0.5\, K/(Wm^{-2})$, the value of λc is about 16. The atmospheric relaxation time scale is around 17 days, the ocean time scale is about 1.5 days, but the coupled time scale is about 325 days, or almost a year. Even in the limit of vanishing water depth, the coupled time scale is about 300 days. For a more realistic ocean mixed layer depth of 50 m, the ocean relaxation time scale is about 70 days and the coupled time scale is about 560 days.

Thus coupling the atmosphere to a surface—even a land surface with vanishing heat capacity—increases the relaxation time scale of the system by at least an order-of-magnitude.

One way to think about this is to recognize that the case of fixed water temperature is the same thing as taking the depth of the ocean slab to be infinite. In essence, the atmosphere relaxes back to the ocean on its atmospheric relaxation time scale. When, at the opposite limit, the depth of the water approaches zero, there can be no perturbation heat flux from the lower boundary (since the lower troposphere is considered opaque in the IR and the solar flux is constant) so the atmosphere must relax purely by internal radiative relaxation: The balance in

(3.37) is then between the relaxation on the left side and the perturbation radiative flux, as represented by the first term in the right side. The time scale is now $\lambda \frac{\Delta p}{g}\left(c_p + \frac{L_v^2 q_s^*}{R_v T_s^2} \right)$, which is the climate sensitivity multiplied by the effective heat capacity of the atmosphere. (At constant relative humidity, the energy needed to heat a sample of air by 1 K includes the energy needed to increase the latent heat content of the sample. With a temperature of 300 K, the latent heat term is more than 5 times the sensible heat contribution to the heat capacity.) For the parameters listed above, this is about 300 days.

In contemplating how the RCE state reacts to perturbations, it is important to keep in mind that both convection and radiation are nonlocal: perturbations at any level can have substantial effects at any other level. In the case of radiation, this is essentially instantaneous an extends through the whole atmosphere. Convection has a response time ranging from hours to days, and so the effect is not instantaneous but is nonlocal through the depth of the convecting layer. One should not think of the reaction to perturbations as constituting anything like a simple Newtonian relaxation.

To illustrate this, we perturb the RCE state of the single-column model by reducing the specific humidity by 70% at 800 hPa, decaying to zero 100 hPa above and below that level, with the ocean temperature fixed. Figure 3.26 shows the response of the model to this rather large perturbation.

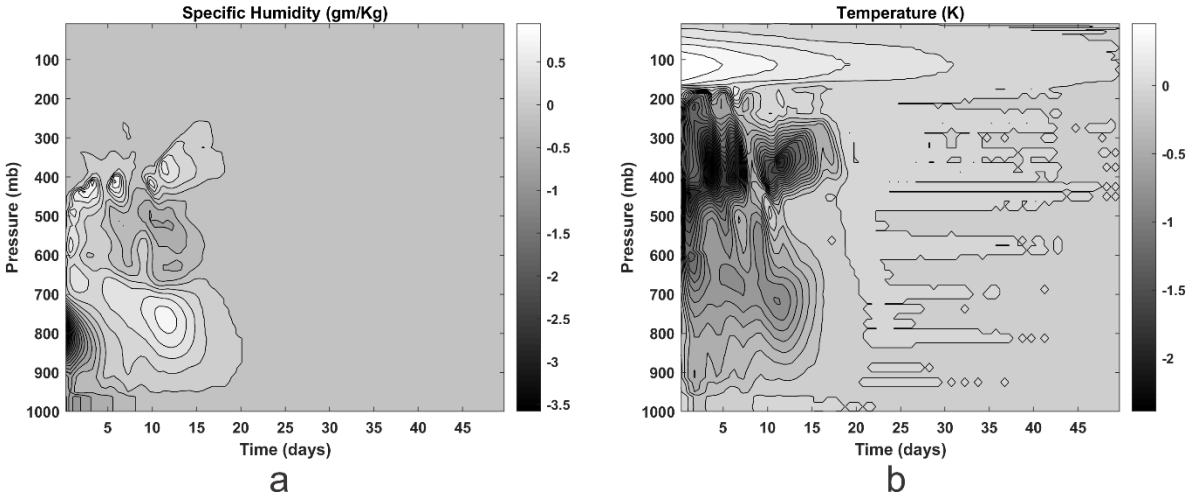

Figure 3.26: Response of the single-column RCE state to a large negative anomaly of water vapor centered at 800 hPa, holding the surface temperature fixed. a) Perturbation specific humidity (g Kg^{-1}); b) Perturbation temperature (K).

Several aspects of the response are particularly interesting. First, far from being Newtonian, the initial water vapor anomaly in the lower troposphere reverses sign on the way to recovery. And, even though the temperature was not perturbed, there is a strong response nonetheless. The initial dry perturbation greatly reduces convective heating, so the column cools, particularly in the upper troposphere. The initial recovery of convection is fairly shallow, leading to excessive moistening of the lower troposphere by day 10, while the upper troposphere continues to cool in the absence of deep convection.

The important point is that the response of RCE states to global perturbations is both nonlocal in altitude and non-Newtonian in time. And, as we saw earlier, the time scale to return to RCE is greatly lengthened by coupling to an interactive surface.

c. Behavior of local perturbations to RCE

Imagine beginning with a moist RCE state and then artificially adding heat to (or subtracting it from) a localized patch of the underlying ocean. This can happen, for example, when ocean currents converge heat into or away from area. Alternatively, the surface winds may change in a particular place, increasing or decreasing the surface enthalpy flux without changing the ocean temperature very much on short time scales.

If the patch of ocean in question is very small, then advection of unperturbed RCE air over the patch would no doubt minimize any response to it. At the other extreme, if the patch is very large, we are effectively back to the global RCE perturbation discussed in the previous section.

In between, at intermediate scales, we would intuitively expect to find more convection and rising air over a warm patch, and sinking air and less convection, or perhaps no convection, over a cold patch.

In either case, the density temperature over the anomalously warm or cold surface cannot depart much from that of the surrounding atmosphere, because of it did, internal waves would quickly eliminate any differences. If the Coriolis parameter is nonzero and the surface patch is not small compared to an internal deformation radius, then rotational dynamics will eventually allow density temperature gradients to build up. Moreover, frictional stresses in the boundary layer can potentially balance pressure gradients, so we would not be surprised to find temperature gradients there.

Yet above the boundary layer, and for surface patches that are much smaller than a deformation radius (which is large in the tropics), we expect that for sufficiently slow systems the density temperature will not vary much on isobaric surfaces and we can use this fact to estimate the response of the atmosphere to the surface perturbations. This approximation, introduced by Sobel and Bretherton (2000), has become known as the *Weak Temperature Gradient* (or "WTG") approximation and it is a very powerful means of understanding quasi-steady circulations in the tropics.

When combined with a method of representing moist convection, WTG allows us to calculate the vertical motion of the tropical atmosphere. The general idea is illustrated in Fig. 3.27.

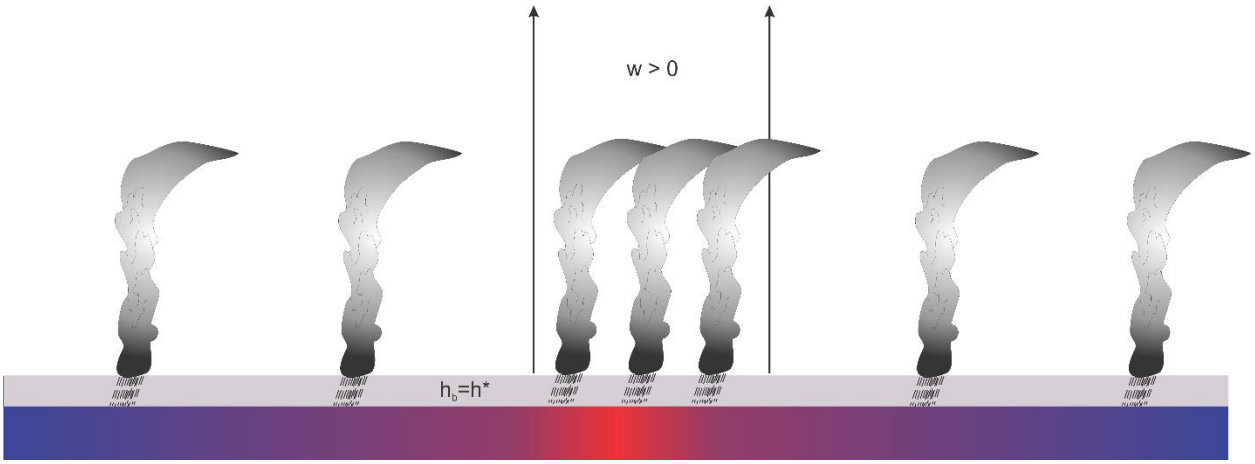

Figure 3.27: Response of an RCE atmosphere to a positive ocean temperature anomaly in the center of the figure. Colored bar at bottom denotes ocean temperature. The gray bar above that represents the subcloud layer, with a moist static energy equal to the uniform value of the saturation moist static energy, h, of the free troposphere. The excess surface enthalpy flux over the warm water causes extra convection, which leads to excess heating of the column. In the WTG approximation, this is offset by the adiabatic cooling associated with large-scale ascent of magnitude w.*

Over the warmer water, assuming that the surface wind speed is not smaller, there will be larger enthalpy flux from the sea. This will drive excess moist convection, which will cause excess heating of the column unless the radiative cooling also increases over the warm patch. Assuming that this is not the case, to obey the WTG approximation, there will have to be just enough large-scale ascent (arrows in Fig. 3.27) so that the adiabatic cooling associate with that ascent just cancels the excess convective heating. Thus application of WTG yields the large-scale ascent.

WTG, coupled with the principle of moist convective neutrality, implies that the subcloud layer moist static energy, h_b is equal to the uniform value h^* of the saturation moist static energy of the troposphere. Neglecting the direct effects of water substance on density, h^* will be constant in the vertical, up to the tropopause, because the troposphere will have a moist adiabatic lapse rate. It will also be constant in the horizontal, according to WTG. Thus the whole tropospheric temperature can be characterized by a single, constant value of h^*.

If the domain is horizontally infinite, than the value of h^* is that of the RCE state. But if the domain has finite dimensions, then h^* will have to be recalculated such that there is gentle, large-scale descent outside the warm patch of sufficient strength to make the domain-average vertical velocity vanish. We will see how to do this presently.

Suppose that, instead, we insert a patch of water in the middle of the domain that is colder than that of the RCE state; this is illustrated in Fig. 3.28.

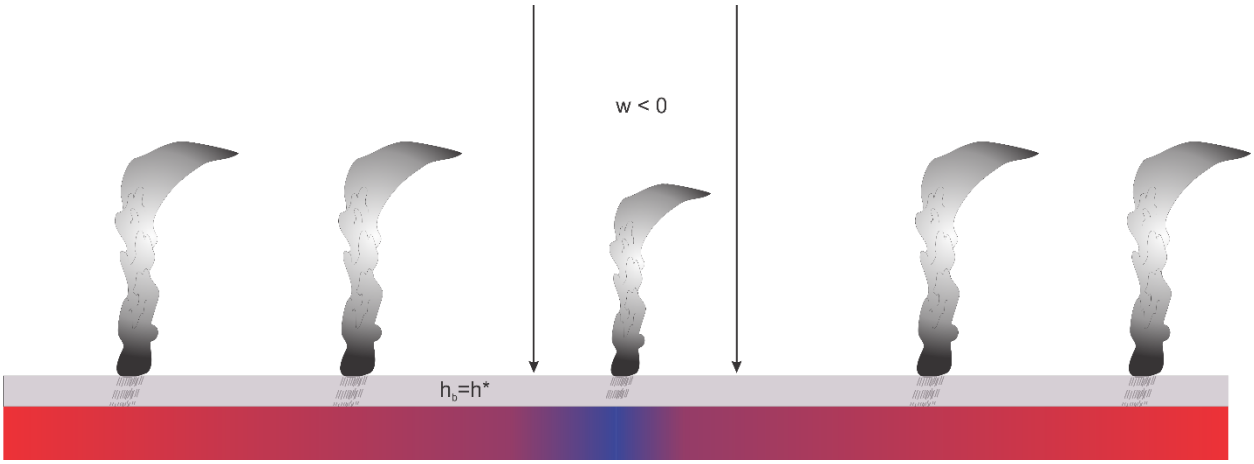

Figure 3.28: As in Fig. 3.27 but with colder water in the middle of the domain.

Now there is descent over the colder water, owing to deficient surface enthalpy fluxes there. If the water is not too cold, the deep convective mass flux will decrease but not vanish, and one can still assume that the atmosphere is convectively neutral, with subcloud layer moist static energy equal to the h^* of the free troposphere. But if the patch is cold enough, relative to the surrounding RCE state, the deep convection shuts off, though shallow convection may remain (Fig. 3.29), and the large-scale descent rate is limited by the balance between subsidence warming and radiative cooling. In this case, convective neutrality cannot apply and the subcloud layer becomes thermodynamically decoupled from the free troposphere. Now we have to solve a rate equation to find the value of the subcloud layer moist static energy.

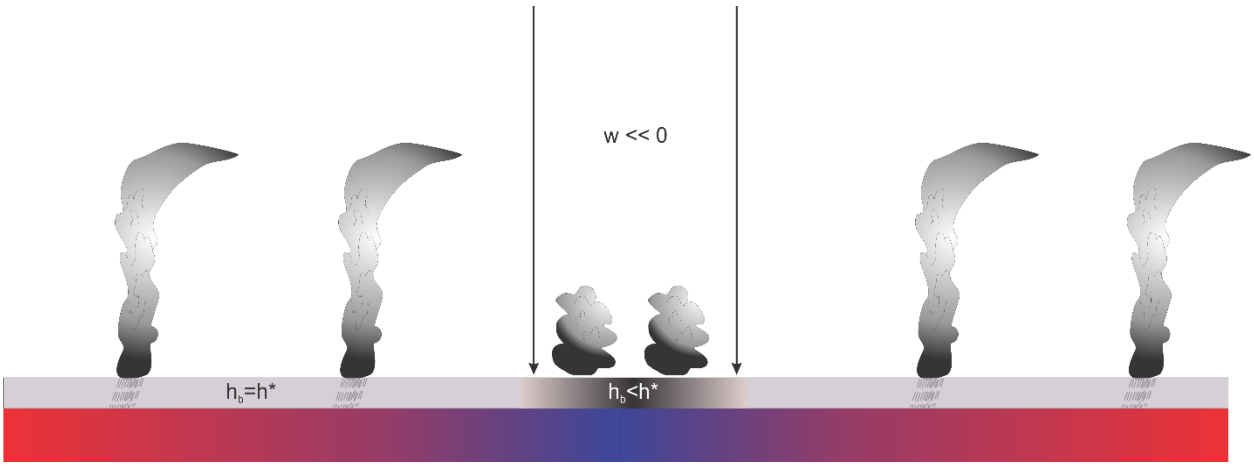

Figure 3.29: As in Fig. 3.28 but with colder water in the center. Deep convection has vanished over the cold water and the large-scale descent rate is that for which subsidence warming balances radiative cooling.

Once we have calculated the vertical velocity everywhere, we can use mass continuity together with the vorticity equation to calculate the entire velocity field. If there is no background vorticity, then no relative vorticity will develop and the resulting horizontal flow will be irrotational. But the full momentum equations can be inverted to find the distribution of pressure in the system, and through the hydrostatic equation, perturbations to the density temperature. The original WTG can, in principle, be modified to include these perturbations and the calculation repeated. For

typical tropical circulations like the Walker circulation, these temperature perturbations amount to a few tenths of kelvins.

If the system has some background vorticity, as is usually the case off the equator, then larger temperature perturbations can build up, particularly if the scale of the surface perturbations is not small compared to a deformation radius. But the same reasoning applies… once the vertical motion has been calculated, the irrotational flow can be calculated from mass continuity and the nondivergent part can then be calculated from the vorticity equation. The momentum equations can then be inverted to find the pressure and thus the density temperature perturbations, and a correction can be made to the original WTG state and the calculation repeated.

The important point here is that for systems for which WTG is a good approximation, dynamics take a back seat to the thermodynamic processes driving the system and the horizontal flows can be estimated from the distribution of vertical velocity. Naturally, the whole system must be dynamically and thermodynamically self-consistent, but the easiest way to think about systems like these is to think about what distribution of large-scale vertical velocity is consistent with the thermodynamic forcing, and then what distribution of horizontal velocity is consistent with that vertical velocity via mass continuity and the momentum equations.

The response of the RCE state to local perturbations can be quantified by marrying the WTG principle with a representation of moist convection. For the latter, we introduce the principle of boundary layer quasi-equilibrium (Emanuel, 1993). This simply maintains that convective activity must be sufficient to remove moist static energy from the subcloud layer at the rate at which surface fluxes and horizontal advection supply it, so that there is no accumulation of moist static energy in the relatively thin subcloud layer.

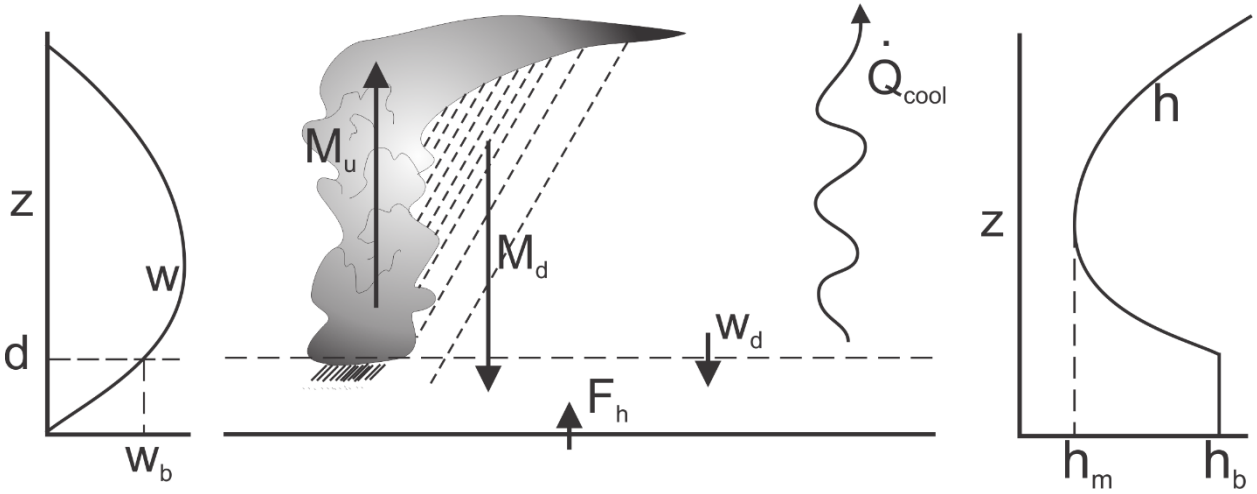

Figure 3.30: Sketch of the principles of boundary layer quasi-equilibrium. The subcloud layer has depth d and moist static energy h_b. A turbulent enthalpy flux F_h transfers enthalpy from the surface to the atmosphere and energy is removed from the troposphere by radiative cooling whose magnitude just above the top of the subcloud layer is $\dot{Q}_{cool}$. A large-scale vertical velocity w has a magnitude w_b just above the top of the subcloud layer. Convective updrafts transport mass upward at a rate M_u while convective downdrafts transport mass downward at a rate M_d and subsidence in the clear air between clouds transports mass into the boundary layer at a velocity w_d. The convective and clear sky downdrafts are assumed to transport moist static energy with a value of h_m into the subcloud layer.

The principles of boundary layer quasi-equilibrium (BLQE) are illustrated in Fig. 3.30. The subcloud layer has depth d and moist static energy h_b . A turbulent enthalpy flux F_h transfers

enthalpy from the surface to the atmosphere and energy is removed from the troposphere by radiative cooling whose magnitude just above the top of the subcloud layer is $\dot{Q}_{cool}$. A large-scale vertical velocity w has a magnitude w_b just above the top of the subcloud layer. Convective updrafts transport mass upward at a rate M_u while convective downdrafts transport mass downward at a rate M_d and subsidence in the clear air between clouds transports mass into the boundary layer at a velocity w_d . The convective and clear sky downdrafts are assumed to transport moist static energy with a value of h_m into the subcloud layer. Note that we define $\dot{Q}_{cool}$ to be positive when there is radiative cooling, and M_d and w_d to be positive downward.

In regions of deep convection, conservation of energy in the subcloud layer can be written

$$d\frac{\partial h_b}{\partial t} = d\mathbf{V}_h \bullet \nabla h_b + \alpha F_h - \left(\alpha M_d + (1-\sigma) w_d\right)\left(h_b - h_m\right) - \alpha \dot{Q}_{cool} d, \tag{3.50}$$

where α is the specific volume, σ is the fractional area covered by deep convection $\mathbf{V}_h$ is the large-scale horizontal velocity in the subcloud layer (assumed constant with height within the layer, as is h_b itself).

At the same time, conservation of mass in the subcloud layer dictates that

$$\alpha\left(M_u - M_d\right) - (1-\sigma) w_d = w_b \tag{3.51}$$

Eliminating the quantity $\alpha M_d + (1-\sigma) w_d$ between (3.50) and (3.51) yields

$$d\frac{\partial h_b}{\partial t} = d\mathbf{V}_h \bullet \nabla h_b + \alpha F_h - \left(\alpha M_u - w_b\right)\left(h_b - h_m\right) - \alpha \dot{Q}_{cool} d. \tag{3.52}$$

The BLQE approximation is just the limit of taking d to be small in (3.52). This can be regarded as a constraint on the convective updraft mass flux:

$$M_u = \rho w_b + \frac{F_h}{h_b - h_m}. \tag{3.53}$$

Note that for positive surface fluxes, $M_u > \rho w_b$, since we take $h_m < h_b$.

Just how good is the BLQE approximation? We can get some feeling for that by comparing the magnitude of the time tendency term in (3.52) with one of the other terms on the right side. For example, For constant surface fluxes in RCE $w_b = 0$, perturbing the boundary layer moist static energy, h_b, in (3.52) gives

$$\rho d\frac{\partial h_b'}{\partial t} = -\overline{M_u} h_b', \tag{3.54}$$

where $\overline{M_u}$ is the mean convective updraft mass flux in RCE, which from (3.24) is given by $\overline{M_u} = \dot{Q}_{cool} / \epsilon_p \mathbf{S}$. It is then evident from (3.54) that the relaxation time scale is given by

$$\tau \sim \frac{\epsilon_p \rho \mathbf{S} d}{\dot{Q}_{cool}}. \tag{3.55}$$

For a subcloud layer depth of 1 km, $\epsilon_p = 0.5$, a temperature lapse rate of $6K\ km^{-1}$, and a radiative cooling of $2K\ day^{-1}$, this works out to be about 1 day. So this would not be a good approximation for dealing with the response of a deep convecting system to the diurnal variation of solar radiation, a point we shall return to shortly. But for steady responses to imposed steady forcing, or forcing varying on time scales more than a few days, (3.53) should work well.

The WTG approximation states that above the boundary layer, the density temperature is constant in horizontal space and time. In the simple model we are building here, this is approximated by constant dry static energy above the boundary layer. Since there are no horizontal gradients, there is no horizontal advection and we can write

$$\frac{\partial s_d}{\partial t} = 0 = -w_d \frac{ds_d}{dz} - \alpha \dot{Q}_{cool} = -w_d \mathbf{S} - \alpha \dot{Q}_{cool}, \tag{3.56}$$

where $s_d \cong c_p T + gz$ is the dry static energy and $\mathbf{S} \equiv ds_d / dz$ is the dry static stability just above the top of the subcloud layer and is also constant under WTG.

Thus from (3.56) and (3.51) we have

$$\rho w_d \mathbf{S} \cong \left(M_u - M_d - \rho w_b \right) \mathbf{S} = \dot{Q}_{cool}, \tag{3.57}$$

where we have made the approximation $\sigma << 1$; alternatively, one could replace $\mathbf{S}$ by $(1-\sigma)\mathbf{S}$.

The downdraft mass flux, M_d, is driven by evaporation of falling precipitation. We represent it here as proportional to the updraft mass flux via (3.23), which we repeat here:

$$M_d = \left(1 - \epsilon_p\right) M_u, \tag{3.58}$$

where ϵ_p is a precipitation efficiency, defined so that $0 \le \epsilon_p < 1$. When $\epsilon_p = 1$, all the precipitation that forms reaches the ground and none re-evaporates, so there can be no deep downdrafts. At the other extreme, when $\epsilon_p = 0$, there is no net latent heat release and the downdraft must be as strong as the updraft. Equation (3.58) just linearly interpolates between these two physical limits.

If we use this formulation for the convective downdrafts in (3.57), then that equation and (3.53) constitute a pair of equations for the updraft mass flux M_u and the large-scale vertical velocity w_b that can be solved together for these two quantities, resulting in

$$\rho w_b = \frac{1}{1 - \epsilon_p} \left[\frac{\epsilon_p F_h}{h_b - h_m} - \frac{\dot{Q}_{cool}}{\mathbf{S}} \right], \tag{3.59}$$

and

$$M_u = \frac{1}{1-\epsilon_p}\left[\frac{F_h}{h_b - h_m} - \frac{\dot{Q}_{cool}}{\mathbf{S}}\right]. \tag{3.60}$$

These should be valid for sufficiently slow variations of surface fluxes and radiative cooling so long as the updraft mass flux given by (3.60) turns out to be nonnegative. It should also be remarked that, according to WTG, the saturation moist static energy $h*$ of the free troposphere is a constant, and since we assume convective neutrality, $h_b\,(=h*)$ must also be constant.

Remember that these solutions pertain to quantities just above the subcloud layer, and are calculated using surface fluxes, radiative cooling that is also evaluated just above the subcloud layer, and moist static energy h_m that represents some weighted average of the moist static energy just above the subcloud layer and that characterizing convective downdrafts. We interpret this here as a value broadly representative of the lower to middle troposphere. As we saw in our very simple model of RCE, that value is ultimately set by precipitation efficiency and static stability. Here we will develop a simplified rate equation for h_m by assuming it is proportional to a deep tropospheric mean moist static energy:

$$h_m = \langle h \rangle \equiv \frac{1}{p_s - p_t}\int_{p_t}^{p_s} h\,dp, \tag{3.61}$$

where p_s and p_t are the pressure at the surface and tropopause, respectively. Henceforth we will use angle brackets, as in (3.61), to denote a mass-weighted vertical average.

To derive a rate equation for $h_m\,(=\langle h \rangle)$, we begin with the general conservation equation for moist static energy:

$$\rho\frac{\partial h}{\partial t} = -\rho\mathbf{V}_h \bullet \nabla h - \rho w\frac{\partial h}{\partial z} - \frac{\partial F_{rad}}{\partial z} - \frac{\partial F_c}{\partial z}, \tag{3.62}$$

where F_{rad} and F_c are the radiative and turbulent fluxes. If we divide (3.62) through by the density ρ and make use of the hydrostatic equation, (3.62) becomes

$$\frac{\partial h}{\partial t} = -\mathbf{V}_h \bullet \nabla h + \rho g w\frac{\partial h}{\partial p} + g\frac{\partial F_{rad}}{\partial p} + g\frac{\partial F_c}{\partial p}. \tag{3.63}$$

Apply the angle bracket operator to this equation yields

$$\frac{\partial h_m}{\partial t} = -\langle \mathbf{V}_h \bullet \nabla h \rangle - G w_b - \langle \alpha \dot{Q}_{cool} \rangle + \frac{g}{p_s - p_t}F_h, \tag{3.64}$$

where

$$G \equiv \frac{1}{w_b}\left\langle -\rho g w\frac{\partial h}{\partial p}\right\rangle. \tag{3.65}$$

The quantity G is referred to as the *gross moist stability* (Neelin and Held, 1987). This quantity plays an important role in the physics of the tropical atmosphere, and its sign and magnitude are

determined by the joint profile of vertical velocity and moist static energy. Since the gradient of the latter changes sign within the deep troposphere, it is not immediate apparent what the sign of G is, and this quantity will at any rate vary in magnitude with conditions. For the remainder of this chapter we shall assume that G is positive, meaning that upward motion reduces the mean moist static energy.

In deriving (3.65) we have assumed that the convective flux of moist static energy vanishes at the tropopause.

The horizontal advection (first term on left of (3.64)) is not necessarily small. Since we assume no horizontal gradients of temperature above the boundary layer, most of this term consists of horizontal advection of moisture. (There may also be a contribution from temperature advection in the boundary layer, where WTG does not apply.) In the tropics, there is nearly always at least an eddy flux of water vapor and this can have a substantial effect on tropical physics through (3.64.) Nevertheless, for the present purpose of a simple conceptual framework, we neglect it in most of the following analysis.

If the equation for the updraft mass flux, (3.60), predicts a negative value, this indicates that deep convection does not occur and we must set $M_u = 0.$ The free tropospheric energy balance then shows that

$$\rho w_b = \rho w_d = -\frac{\dot{Q}_{cool}}{\mathbf{S}} \quad \text{if} \quad M_u = 0. \tag{3.66}$$

The steady-state form of (3.52) must then be solved for the subcloud payer moist static energy:

$$d\mathbf{V}_h \bullet \nabla h_b + \alpha F_h + w_d \left(h_b - h_m \right) - \alpha \dot{Q}_{cool} d = 0, \tag{3.67}$$

with w_d given by (3.66). But to solve this, one needs the value of moist static energy in the free troposphere, h_m. Although (3.64) is still technically valid, evaluating the gross moist stability G in this case would be difficult as the distribution of moist static energy is no longer being controlled by deep moist convection. Referring to Fig. 3.29, The only source of water above the boundary layer in this case would be advection from nearby regions of deep convection. But we can place a firm lower bound on h_m : the value it would have if the concentration of water were zero:

$$\left(h_m \right)_{min} = h^* - L_v q^*, \tag{3.68}$$

and clearly this would reach a minimum value just above the top of the subcloud layer. The value of q* would correspond to the temperature of the free troposphere in the regions of deep convection, according to WTG. If the surface fluxes and radiative cooling of the subcloud layer are known, then (3.68) can be used with (3.67) to solve for the subcloud layer moist static energy.

To summarize, our simple system consists of (3.59), (3.60) and (3.64), if M_u turns out to be positive, and (3.66)-(3.68) otherwise. This assumes that the surface enthalpy flux, radiative cooling, and precipitation efficiency can be specified or determined as functions of the other variables.

It is worth nothing that the only time dependence in this system comes in through the deep tropospheric moist static energy budget, (3.64). Even for a fixed ocean temperature, this is a long time scale, equivalent to the RCE atmospheric relaxation scale given by (3.44) – around 20 days. This is well more than the boundary layer relaxation time scale of around 1 day given by (3.55). We will see just how important this time scale is later in this chapter.

So we return to the problem illustrated in Figs 3.27-3.29: The response of a horizontally infinite RCE atmosphere to a localized patch of anomalous surface enthalpy flux. To keep things simple, we hold the radiative cooling, gross moist stability, and precipitation efficiency constant and ignore horizontal advection in (3.64) and (3.67). We seek steady solutions and thus set the time derivative term in (3.64) to zero; this together with (3.59) and (3.60) constitute our system.

There is a circumstance in which such a solution is not viable. According to the steady form of (3.64), the solution for w_b will always be finite for finite radiative cooling and surface flux, but (3.59) indicates that w_b blows up in the limit of unitary precipitation efficiency $\left(\epsilon_p = 1\right)$ unless the quantity in brackets on the right side of (3.59) vanishes too. But this cannot happen for sufficiently large surface flux because h_b is fixed and there is a definite lower bound to the value of h_m. Thus, under this circumstance, there is an upper bound to the surface enthalpy flux, F_h, for the solution to be viable.

To see which circumstance leads to a bound on the surface flux, we can look at the solution for the column relative humidity (CRH) in the limit of large surface fluxes. Here we define CRH as

$$CRH \equiv 1 - \frac{h^* - h_m}{\mathbf{S}H}. \tag{3.69}$$

With this definition, when the atmosphere is saturated $\left(h^* = h_m\right)$, $CRH = 1$, and when the moist static energy of the troposphere has a value corresponding to vanishing specific humidity, $CRH = 0$. Solving for $h^* - h_m$ using (3.59) and the steady form of (3.64) in the limit of large surface fluxes gives

$$\lim_{F_h \to \infty} \left(CRH\right) = 1 - \frac{G}{\mathbf{S}} \frac{\epsilon_p}{1 - \epsilon_p}. \tag{3.70}$$

The fact that this limiting value of column relative humidity should not be less than zero restricts the last term in (3.70) to be less than 1. This will not be possible for value of ϵ_p sufficiently close to 1.

In reality, it is unlikely that the last term on the right side of (3.70) will exceed unity. Precipitation efficiency is likely to be large only in a sufficiently humid atmosphere, for which the value of G will be small (G vanishes in a saturated atmosphere with a moist adiabatic lapse rate).

But (3.70) does show that *CRH* remains less than 1 even in the limit of large surface fluxes as long as G and ϵ_p are positive.

With that said, Fig. 3.31 shows solutions to the system for $\epsilon_p = 0.5$, $\alpha \dot{Q}_{cool}$ equivalent to $1\,K\,day^{-1}$, $p_s - p_t = 800\,hPa$, $\mathbf{S} = 3.5\,ms^{-2}$ and $G = 0.2\mathbf{S}$. For these values of the parameters, the RCE surface enthalpy flux is $94\,W\,m^{-2}$.

Deep convective mass fluxes vanish when the surface enthalpy flux falls below about $80\,W\,m^{-2}$, and the vertical velocity in the absence of convection has a magnitude of around $3\,mm\,s^{-1}$. Otherwise, both the mass fluxes and vertical velocity increase linearly with the surface enthalpy flux. The degree of subsaturation, $h^* - h_m$, has its maximum value in the region devoid of deep convection, and this value corresponds (by assumption) to the complete absence of water vapor. Otherwise, the subsaturation diminishes with increasing enthalpy flux and therefore with increase convective mass flux, as expected. The column relative humidity is zero, by assumption, in the absence of dep convection and increases with enthalpy flux, approaching the asymptotic value given by (3.70) at large forcing.

Precipitation increases rapidly with column humidity (Fig. 3.31d), with the slope asymptoting to infinity at large forcing, because of the bounded value of column humidity. A similar relationship is observed in nature (Fig 3.32). This observed relationship is widely interpreted as indicating a direct sensitivity of convective plumes to water vapor, but the model we are using here has no direct dependence of convection on free tropospheric water vapor. Thus the data in Fig 3.32 should not be interpreted as necessarily implying any such dependence. Nevertheless, it is undoubtedly the case that moist convection is sensitive to moisture, and in our simple model, this would enter through a dependence of the precipitation efficiency $\left(\epsilon_p\right)$ on humidity. Allowing ϵ_p to increase with humidity would yield an even greater sensitivity of precipitation to column humidity, according to (3.59) and (3.60).

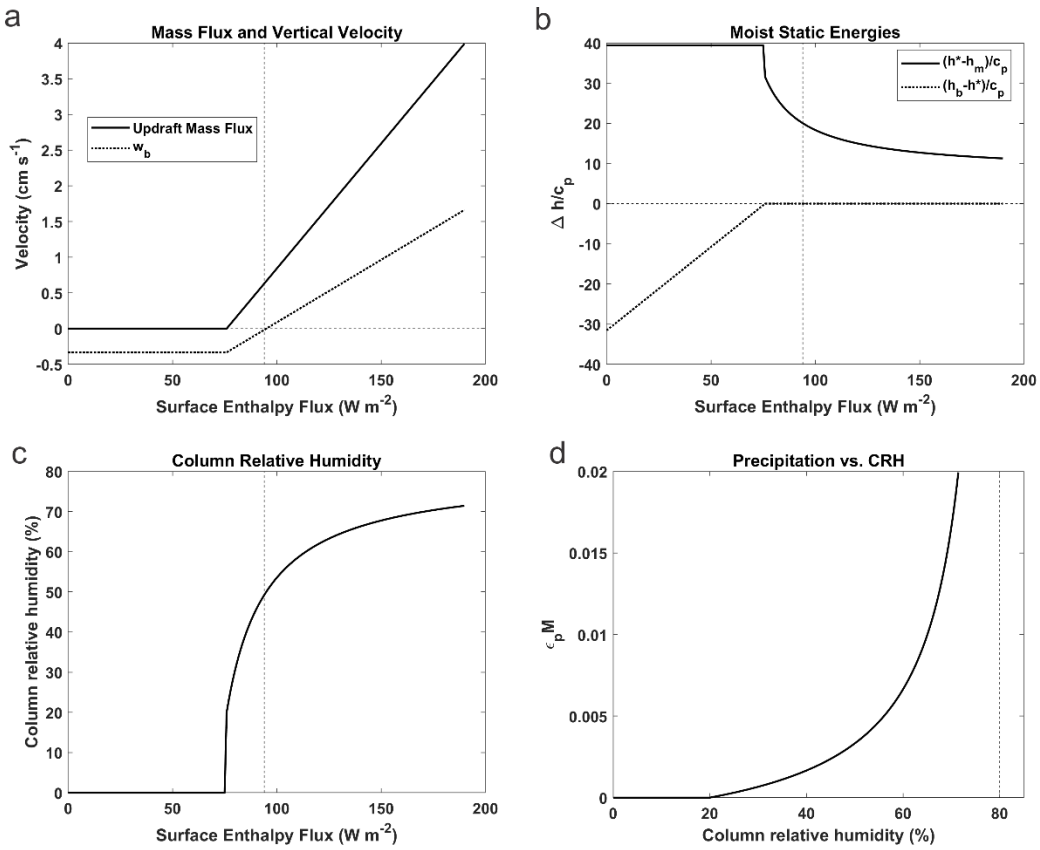

Figure 3.31: Response of a horizontally infinite RCE atmosphere to a local patch of anomalous surface enthalpy flux. The large-scale vertical velocity and convective updraft mass flux (normalized by air density) are shown in a). The differences between the actual and saturation moist static energies of the free troposphere and between the boundary layer moist static energy and the saturation moist static energy of the free troposphere, both normalized by heat capacity, are shown in b). The column relative humidity is shown in c) and a proxy for precipitation (updraft mass flux multiplied by precipitation efficiency) is graphed against column humidity in d). The RCE value of the surface enthalpy flux in indicated in a)-c) by the vertical dashed line. In d) the vertical dashed line indicates the asymptotic value of column relative humidity as the surface enthalpy flux gets very large. See text for values of the parameters used here.

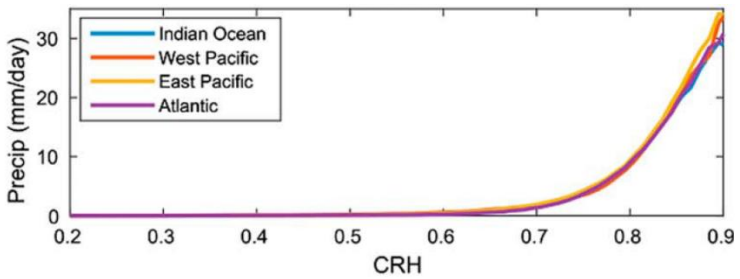

Figure 3.32: Observed mean precipitation in 1% bins of column relative humidity for tropical ocean basins using version 7 SSM/I satellite-derived products over the period 1998–2001.

We can also examine the response of RCE to local perturbations by modifying the single-column model described earlier in this chapter. This follows the concept described in detail in Sobel and Bretherton (2000). We first run the single-column model into a state of RCE, as usual. We then restart the model from its RCE state but do not permit the temperature above a specified pressure level to change and specify a higher or lower sea surface temperature than the RCE state. At each time step, the sum of the convective and radiative heating is calculated at each level. To maintain energy balance at each level, a vertical velocity is calculated such that the adiabatic cooling or warming associated with that velocity is just sufficient to offset the sum of the convective and radiative heating. That vertical velocity is then used to advect water vapor in the vertical direction. As with the RCE calculation, the integration is run until the variables reach statistically stable values. (This feature is built into the model available on the course web page.)

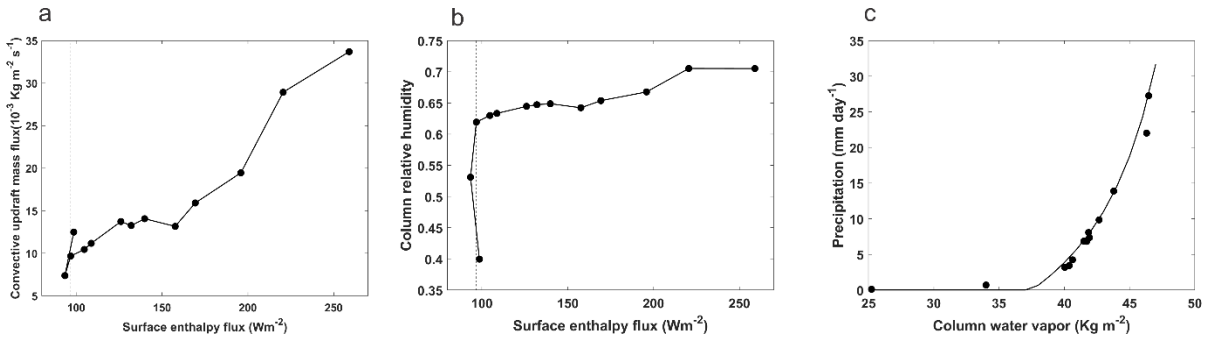

Figure 3.33: Response of the single-column model run with temperature fixed at its RCE value and vertical motion calculated to enforce local thermodynamic balance. Sea surface temperature is varied from -0.5 K to 3.5 K relative to its RCE value. a) shows the convective updraft mass flux as a function of the surface enthalpy flux. The variation of column relative humidity with surface flux is shown in b) and the variation of precipitation with column humidity is shown in c). The curve in c) is a fit of the toy model to the data. The RCE value of the surface enthalpy flux is indicated by the vertical dashed line in a) and b).

An example of the response of the single-column model to sea surface temperature anomalies ranging from -0.5 K to 3.5 K, relative to its RCE value, is shown in Fig. 3.33. When the SST anomaly is -0.5 K only small trade cumuli are present and the net vertical motion is downward. Unlike in the analytical model just described, the column does not completely dry out, because the single-column model assumes that convergence into the column is from an adjacent column in RCE and carries with it the water vapor content of the RCE column.

When the SST anomaly is -0.25 K, the dominant mode of convection is cumulus congestus that extend up to 600 hPa and which do weakly precipitate.

As expected, the net vertical motion is upward for all positive SST anomalies and the convective mass flux increase nearly monotonically with surface fluxes (Fig. 3.33a). However, the column moistens only very slowly (Fig. 3.33b). Precipitation climbs steeply with column humidity (Fig. 3.33c) and a fit of the analytical model (using constants that best fit the single-column model output) works well.

Surprisingly, upward and downward motion may arise spontaneously in the single-column model run in WTG mode even when no surface temperature anomaly is imposed, suggesting a fundamental instability of the RCE state. This is examined in the next section. But before

proceeding, we note two important limitations of applying and/or interpreting tropical atmospheric physics using this framework.

The first is a caution against regarding either the surface enthalpy flux or the SST as legitimate externally specifiable parameters. This works on time scales short compared to the adjustment time scale of the ocean surface mixed layer (given by (3.45), around 70 days for typical mixed layer depths), but for longer time scales the ocean-atmosphere system must be regarded as coupled. In the absence of enthalpy advection within the ocean, the surface enthalpy flux must equal the net (shortwave plus longwave) surface radiative flux. In the tropics, where the high infrared opacity of the lower atmosphere prevents much net longwave flux, solar flux will be the main influence on the net surface radiative flux.

Married with the WTG framework discussed in this section, this coupling to radiation can give rise to interesting phenomena, such as climate hysteresis. Referring to Figure (3.29), if a patch of seawater of dimensions less than the local radius of deformation were to become cool enough, not only would deep convection cease, but stratocumulus clouds would form near the top of the boundary layer (see Chapter 4). This would greatly reduce the solar flux and, owing to the requirement of energy balance in the ocean mixed layer, thereby reduce the surface turbulent enthalpy flux. This would reinforce the cold SST anomaly, possibly leading to two stable solutions: One with no SST anomaly and one with low SST and stratocumuli. (But note that there would be a dynamical response to the cold anomaly within the ocean itself, possibly mitigating this effect.)

The second caution has already been pointed out: The framework only works if the subcloud layer can be assumed to be in energy balance. As the relaxation time scale for subcloud layer moist entropy is about 1 day (see (3.55) and subsequent discussion), the diurnal cycle in too fast for BLQE to apply. Nevertheless, we can learn something about the diurnal cycle by gently relaxing BLQE and applying a periodic cycle of surface fluxes driven by the diurnal cycle of insolation. That is, instead of rigorously enforcing BLQE we relax that actual convective updraft mass flux, M_u, back towards it equilibrium value according to

$$\frac{\partial M_u}{\partial t} = \frac{M_e - M_u}{\tau}, \tag{3.71}$$

where

$$M_e \equiv \rho w_b + \frac{F_h}{h_b - h_m}. \tag{3.72}$$

is the BLQE mass fluxes and τ is a boundary layer response time scale given by (3.55). This just relaxes the convective mass flux towards its equilibrium value over the time scale τ. We assume that the land area has a length scale much less than the deformation radius, so that WTG applies, so that, combining (3.57) with (3.58) we have

$$\epsilon_p M_u = \rho w_b + \frac{\dot{Q}_{cool}}{\mathbf{S}}. \tag{3.73}$$

We can eliminate ρw_b between (3.72) and (3.73) and write (3.71) as

$$\tau \frac{\partial M_u}{\partial t} + \left(1-\epsilon_p\right) M_u = \frac{F_h}{h_b - h_m} - \frac{\dot{Q}_{cool}}{\mathbf{S}}. \tag{3.74}$$

To get an analytic solution, we will make a few simplifying assumptions. First, since the time scale for adjustments of the free tropospheric moist static energy, h_m, is on the order of 20 days, we will assume that it remains constant over a diurnal cycle. Second, we assume that the radiative cooling rate, $\dot{Q}_{cool}$, is constant, and the static stability $\mathbf{S}$ is anyway constant under WTG. Finally, we will specify the surface fluxes as a constant needed to balance the radiative cooling plus a specified small perturbation varying on a diurnal time scale and likewise assume that M_u and h_b consist of a mean (RCE) part plus a small perturbation. Then linearizing (3.74) gives

$$\tau \frac{\partial M_u'}{\partial t} + \left(1-\epsilon_p\right) M_u' = \frac{F_h' - h_b' \; \dot{Q}_{cool} / \epsilon_p \mathbf{S}}{\overline{h_b} - \overline{h_m}}, \tag{3.75}$$

where the primes denote the perturbation quantities, the overbars denote RCE values, and we have made use of $\overline{M_u} = \dfrac{\dot{Q}_{cool}}{\epsilon_p \mathbf{S}}$ from (3.73).

Likewise, we linearize (3.52) about the RCE state, ignoring horizontal advection and radiative cooling in the boundary layer, resulting in

$$\rho d \frac{\partial h_b'}{\partial t} + \frac{\dot{Q}_{cool}}{\epsilon_p \mathbf{S}} h_b' = F_h' - \left(\overline{h_b} - \overline{h_m}\right)\left(1-\epsilon_p\right) M_u'. \tag{3.76}$$

Thus (3.75) and (3.76) are a coupled linear system for the perturbation convective updraft mass flux and boundary layer moist static energy, given specified diurnal surface enthalpy flux F_h'. This is only strictly valid for a diurnal cycle that is a small perturbation to the RCE state, which is not usually the case, but we might learn something from this in spite of this restriction.

Notice first that if we multiply (3.75) by $\overline{h_b} - \overline{h_m}$ and subtract (3.76) from the result, making use of (3.55) for τ, the result is

$$h_b' = \frac{\epsilon_p \mathbf{S}}{\dot{Q}_{cool}} M_u'. \tag{3.77}$$

Thus the convective mass flux tracks the boundary layer moist static energy. Loosely speaking, the convection peaks during the hottest part of the day.

If we specify a simply, periodic forcing that peaks at noon local time:

$$F_h' = F_0 \cos(\omega t), \tag{3.78}$$

where ω is the diurnal frequency $2\pi/(1\,day)$, the solution of (3.75) and (3.76) is

$$M_u' = \frac{F_0}{2-\epsilon_p \quad \overline{h_b} - \overline{h_m}} \cos(\omega t - \theta), \tag{3.79}$$

where θ is the phase of the response, given by

$$\tan(\theta) = \frac{\omega\tau}{2-\epsilon_p}, \tag{3.80}$$

with τ given by (3.55). The solution for the boundary layer moist static energy is then given by (3.77).

According to (3.79), the diurnal cycle of moist convection will be stronger when the free troposphere is moist and when there is large precipitation efficiency. The convective available potential energy (CAPE) scales with h_b', given by (3.77) and (3.79), will also be larger in a more humid atmosphere with larger precipitation efficiency and in an atmosphere with large dry static stability and smaller radiative cooling rate. Given a typical value of the boundary layer relaxation time scale τ of about a day, the phase lag given by (3.80) is around 5 hours, depending also on the precipitation efficiency.

From this line of reasoning, we expect strong diurnal cycles of convection in moist atmospheres over land areas whose dimensions are small compared to the local radius of deformation but not so small that horizontal advection in the boundary layer damps the diurnal response of the land by importing cooler air from over the sea. (A sea breeze of $5\,ms^{-1}$ would cross a peninsula of 100 km width in about 5 hours). We expect high CAPE (large h_b') to be associated with lightning, and a glance at the climatological lightning map (Figure 3.9) shows large activity in places like Florida and Cuba (dimensions small compared to the local deformation radius but not much smaller than 100 km or so) and equatorial locations like central Africa.

One takeaway from this is that the diurnal cycle, being too fast for BLQE, allows CAPE to build up and then be released, giving strong convection late in the afternoon. But for the remainder of this book we will concern ourselves mostly with phenomena on time scales much longer than a day for which convective quasi-equilibrium is a good approximation. We next turn to the interesting question of whether RCE states (without diurnal cycles) are actually stable.

3.4 Stability of RCE and the aggregation of tropical convection

Throughout this chapter we have emphasized the value of treating RCE as a starting point for understanding the tropical atmosphere. But is the RCE state stable? Given that RCE is a statistical equilibrium, we can ask whether the statistics remain invariant in time and space or whether, to the contrary, perturbations to that state can amplify and transform it into state with large horizontal and/or time variations in the convective and radiative statistics.

It turns out that under some circumstances, yet to be fully delineated, statistically homogenous RCE states break down spontaneously into clusters whose horizontal scales are many times the typical spacing between cumulus clouds in RCE. With a large enough Coriolis parameter, these clusters take the form of tropical cyclones. *Self-aggregation* of moist convection, as the phenomenon has come to be known, was first discovered in non-rotating cloud-permitting numerical simulations of RCE, first in two dimensions (Held et al., 1993) and a few year later in three dimensions (Tompkins and Craig, 1998). A good review of self-aggregation in numerical models is provided by Wing et al. (2017).

Figure 3.34 shows what non-rotating self-aggregation looks like in a cloud-permitting numerical simulation. This simulation was performed with using a cloud-permitting model, the System for Atmospheric Modeling (SAM; Khairoutdinov and Randall, 2003), run with a horizontal grid spacing of 3 km and a stretched vertical grid, with periodic boundary conditions in both horizontal dimensions. A uniform sea surface temperature (SST) of 305 K was imposed, and a full radiation scheme was used but with time-invariant insolation. The model state was initialized with vertical profiles from a previous integration of the model in a domain too small to permit self-aggregation. (For details see Wing and Emanuel (2014).)

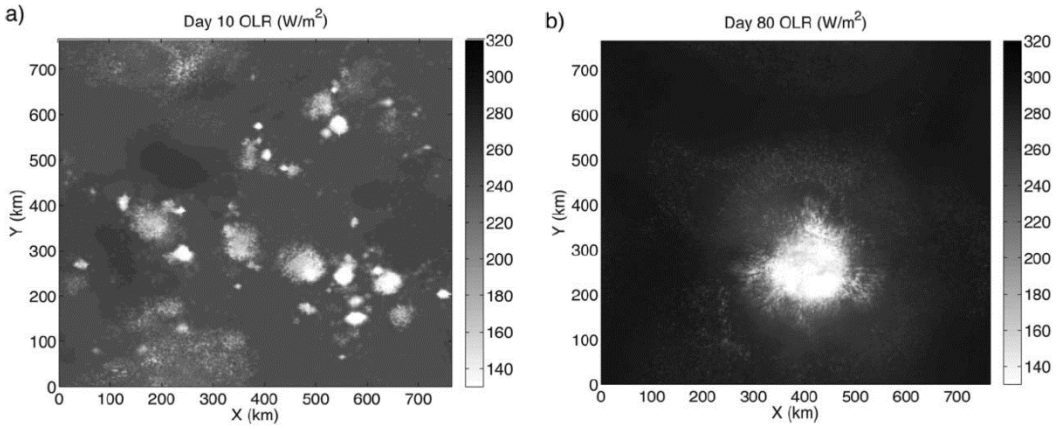

Figure 3.34: Snapshots of outgoing longwave radiation (OLR) in a cloud-permitting simulation of moist convection over an ocean surface of constant temperature at 10 days into the simulation (a) and at 80 days (b). From Wing and Emanuel (2014).

Initially, the convection is fairly randomly distributed in space and time (Figure 3.34a). If the numerical domain is large enough and certain other conditions are satisfied, the convection begins to clump together, and over a period of a few tens of days collapses to a single cluster, as shown in Figure 3.34b. The cluster typically occupied a few tens of percent of the domain, independent of domain size of the domain is square and not too large. Virtually all the rain occurs within the cluster, and the air outside the cluster is extremely dry above the boundary layer, as shown in Figure 3.35 taken from a similar, previously published simulation (Bretherton et al., 2005).

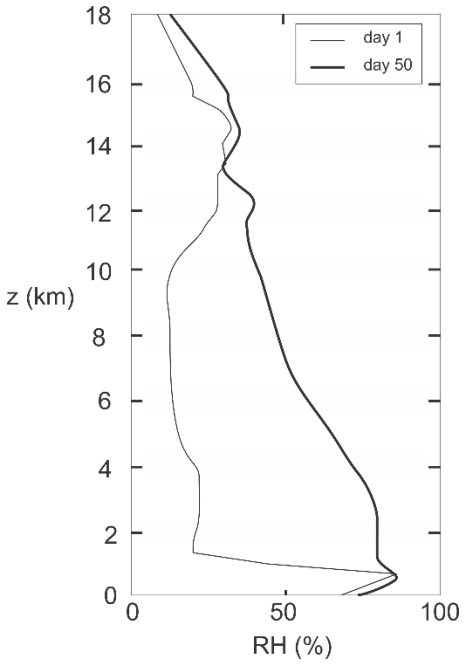

Figure 3.35: Vertical profile of horizontally domain averaged relative humidity at 1 day (thin) and 50 days (thick) into an integration of a cloud-permitting model (Bretherton et al., 2005).

Although the cluster shown here is roughly circular, in other simulations the aggregation takes the form of wavy lines ((e.g. Tompkins and Craig, 1998; Wing and Cronin, 2016). As of this writing, there is no generally accepted theory for the scale of clusters in non-rotating aggregated convection. In the case of rotating self-aggregation, there are well defined scales and these will be discussed in Chapter 15 on tropical cyclogenesis.

As mentioned earlier in this chapter, clusters of deep convective clouds are often observed, both within and outside the tropics (see, e.g., Figure 3.7) but it is difficult to determine whether they arise spontaneously or are associated with pre-existing disturbances.

Why should deep moist convection spontaneously aggregate? To get some insight into this important question, we first note again that in the aggregated state the column-integrated moisture content outside the cluster is relatively small (see Figure 3.35) whereas within the cluster is nearly saturated (not shown). Thus the horizontal variance of the column-integrated moisture is larger than that of the non-aggregated state, where the humidity outside of clouds is much larger.

Given that temperature perturbations in non-rotating convective states are very small, these large moisture excursions will strongly dominate horizontal fluctuations of the moist static energy. Thus the horizontal variance of column moist static energy is larger in the aggregated than in the disaggregated state. Column moist static energy has the very useful property that it is *not directly affected by convection*, which is an energy transfer process and not a source or sink of moist static energy. Thus the only way to change the variance of moist static energy is by the external energy sources of radiative heating and turbulent surface fluxes, and also by large-scale advection. To see this, we begin, following a development closely parallel to (3.61)-(3.65) by writing the equation for conservation of moist static energy in pressure coordinates, assuming that the cluster-scale flow is hydrostatic:

$$\frac{\partial h}{\partial t} = g\frac{\partial F_r}{\partial p} + g\frac{\partial F_t}{\partial p} - \omega\frac{\partial h}{\partial p} - \mathbf{V_h}\bullet\nabla_h h, \tag{3.81}$$

where h is the moist static energy, F_r and F_t are respectively the upward radiative and turbulent fluxes (both assumed to be in the vertical direction only), ω is the total time derivative of pressure, and $\mathbf{V_h}$ is the horizontal velocity vector.

We next define a column integral operator acting on any scalar a:

$$\hat{a} \equiv \frac{1}{g}\int_{p_{tr}}^{p_0} a dp', \tag{3.82}$$

where p_0 is the surface pressure and p_{tr} is the pressure at the tropopause. We assume that the large-scale vertical velocity w and the turbulent fluxes F_t both vanish at the tropopause and apply the integral operator (3.82) to (3.31) to arrive at

$$\frac{\partial \hat{h}}{\partial t} = F_{r0} - F_{tr} + F_{t0} - \omega\frac{\partial h}{\partial p} + \mathbf{V_h}\bullet\nabla_h h, \tag{3.83}$$

where F_{r0} and F_{tr} are the upward radiative fluxes at the surface and tropopause, respectively, and F_{t0} is the surface turbulent enthalpy flux (equivalent to the moist static energy flux). The last two terms in (3.83) represents the advective export of moist static energy from the column. Since horizontal gradients are often (but not always!) weak in the tropics, we usually neglect the last term in (3.83). We recognize G as a slightly different form of the gross moist stability defined by (3.65):

$$G_i \equiv -\frac{1}{\hat{\omega}}\omega\frac{\partial h}{\partial p} = \left(p_0 - p_{tr}\right) G, \tag{3.84}$$

where G was defined by (3.65). The gross moist stability is an $\omega-$weighted vertical integral of the vertical gradient of moist static energy. Since h almost always has a minimum value somewhere in the middle troposphere, the sign of G_i is not *a priori* obvious. It can be, in general, a function of horizontal space and time.

In the long-time average RCE state, there is no time tendency or large scale advection of the column moist static energy, so we have the classical balance $F_{r0} - F_{tr} + F_{t0} = 0$. We consider fluctuations around this equilibrium state and denote these by primes. With these definitions, neglecting the last term in (3.83), and multiplying (3.83) through by $\hat{h}'$ yields an equation for the evolution of the variance of the column moist static energy:

$$\frac{1}{2}\frac{\partial \hat{h}'^2}{\partial t} = \hat{h}'F_{r0}' - \hat{h}'F_{tr}' + \hat{h}'F_{t0}' + G_i\hat{\omega}'\hat{h}', \tag{3.85}$$

where for this purpose we have neglected time variations of G_i.

Self-aggregation of convection is observed (in models) to be accompanied by a strong increase in the variance of column moist static energy, so during aggregation the left side of (3.85) will be positive. Therefore, the right side must also be positive, and this requires fluctuations of the column moist static energy to be positively correlated with one or more of the following:

1. Fluctuations of the net radiative heating of the column, as given by the sum of the first two terms on the right side of (3.85),
2. Fluctuations of the surface enthalpy flux,
3. Fluctuations of $\hat{\omega}$, if G_i is positive.

That is, perturbations to the RCE state may amplify if net tropospheric radiative heating increases with column moisture (positive $\hat{h}'$) or if there are greater surface fluxes where $\hat{h}'$ is elevated (and/or less surface flux where $\hat{h}'$ is depressed). The last term in (3.85) would be positive if there were a net downward motion (positive $\hat{\omega}$) where the column is anomalously moist and/or upward motion where it is dry. This is not usually the case in the kind of aggregation illustrated in Figure 3.34, where the moist columns are ascending and the dry air is descending, but can transiently make a positive contribution. Thus in this case, and in most cases examined to date, the last term in (3.85) is usually a damping term and acts against the aggregation. But there may be places and times where the gross moist stability G_i is negative, and this would indicate a direct feedback between moistening by convection and large-scale ascent.

An important result of this analysis is that the perturbations to column moist static energy may grow only if there are interactions involving radiation and/or surface enthalpy fluxes; barring negative G_i, direct interactions between convection and larger-scale circulations *per se* are stable and cannot "cause" circulation systems to amplify, at least as measured by the variance of column moist static energy. Indeed, most of the studies undertaken with three-dimensional cloud-permitting models (e.g. those reviewed by Wing et al. (2017)) show no self-aggregation when both surface fluxes and radiative heating are horizontally homogenized at each level.

It should be noted that this does not prohibit the growth of disturbances in non WTG-conditions in which column temperature and column water vapor perturbations may both grow but cancel out in their contributions to moist static energy.

Figure 3.36 shows the evolution over time of the values of terms like those on the right side of (3.85), averaged over the domain, for a simulation like that used to construct Figure 3.34. All the terms except for the last term of (3.85) have been calculated directly from the model output, but the last term (the advective term) is difficult to calculate from output that is sparse in time, so has been instead estimated as a budget residual of (3.85).

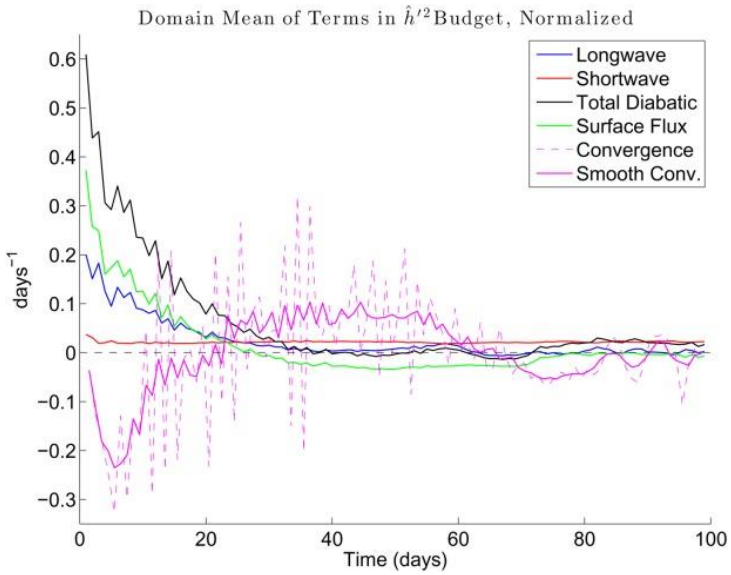

Figure 3.36: Domain averages of the budget terms in the column moist static energy variance equation (3.85), as a function of time from initialization with an RCE state. The first two terms on the right of (3.85) are combined into a radiative term and then split between shortwave (solar) and longwave (terrestrial) components, indicated respectively by the blue and red curves. The term involving surface enthalpy fluxes (third term on right of (3.85)) is shown in green, and the sum of all the diabatic terms is on black. The advective term (last term in (3.85)) is in magenta; it has been derived as a budget residual and the time-smoothed values are indicated by the solid magenta line. From (Wing and Emanuel, 2014)

Initially, all the budget terms except the advective term are positive, indicating positive feedbacks between the amplifying circulation and radiation and convection. Among the larger positive feedbacks in from surface enthalpy fluxes. Column moist static energy is elevated in the emerging convective cluster, and downdrafts associated with the enhanced deep convection create gusts of wind at the surface, which enhance the surface fluxes. (Note that this cannot happen over land, as the land surface has essentially no heat capacity…the first and third terms on the right of (3.85) must cancel to insure no net heat exchange with the soil. In that case, the remaining diabatic term is approximately equal to fluctuations in the net top-of-the-atmosphere radiation.)

The longwave radiative term in of the same order of magnitude as the surface flux term, and more detailed analysis of the simulations reveals that this is dominated by water vapor perturbations early in the simulation. Most of this feedback is manifest in the simulations by developing dry patches emitting more infrared radiation from the surface and boundary layer water vapor, leading to net radiative cooling of the column. Later in the simulations, longwave trapping by the thick, high anvil ice clouds associated with the deep convective cluster dominate the feedback.

There is some direct absorption of sunlight in the atmosphere, mostly by water vapor bands (see Figure 2.5). As there is more moisture in the convective cluster, there can be more absorption of sunlight there (unless there is too much additional reflection by the clouds) and less absorption in the dry patches, so this is usually a positive feedback, as evident in Figure 3.36. (This effect might be expected to be stronger at higher temperatures, owing to the greater concentrations of water vapor.)

But note that around day 30, the sign of the various contributions reverses, with the diabatic terms all putting a break on the increase in variance and the advective term now driving the increase.

Under what circumstances does aggregation occur, and what drives it? To get some insight into these questions, we first consider the effects of water vapor feedback all by itself, and put aside from the moment the important feedbacks between clouds and radiation and surface fluxes and convection.

We begin by inquiring about the response of radiation to drying of a patch of air in the RCE state. The reduction of water vapor, an important greenhouse gas, causes a decrease in both the absorption and emission of infrared radiation by the dry sample. But because, in RCE, most of the troposphere is warmer than it would be in radiative equilibrium (see Figure 3.19), reducing the emission is the larger effect and the sample warms. At the same time, since the sample is emitting less infrared radiation, there is less of it to absorb by greenhouses gases above and below the level of our sample. Thus those samples cool.

This effect is illustrated in Figure 3.37, which shows the response throughout the troposphere to the imposed drying at a particular level (abscissa) in RCE states simulated with the single-column mode (SCM) described earlier in this chapter and available through the course website.

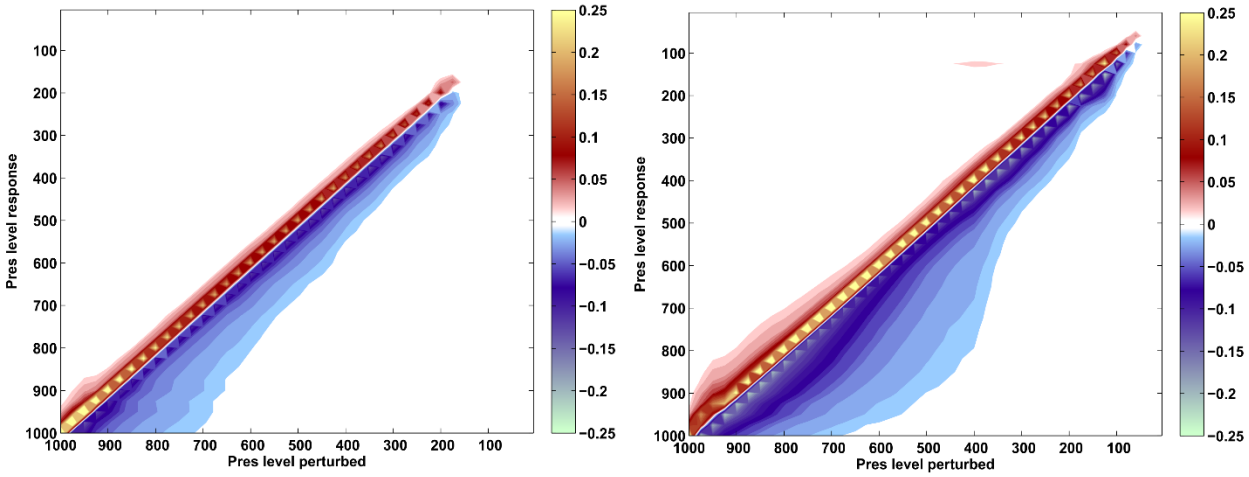

Figure 3.37: Perturbation heating rate as a function of pressure (ordinate) and the pressure level of a 20% negative perturbation in specific humidity (abscissa) to and RCE state, for SSTs of (left) 25°C and (right) 40°C. Plotted is the logarithm of 1 + the actual heating rate, for positive heating rates, and minus the logarithm of 1 minus the heating rate, for negative heating rates. Figure and caption from Emanuel et al. (2014).

The left side of the figure is for an RCE state with a fixed SST of 25°C while the right side is for 40°C. The diagonal red streak shows that drying the parcel reduces the radiative cooling of the parcel itself, while the blue shows that air below the dried parcel level is anomalously cooled owing to the reduced downward infrared flux from the dried sample. (Note that the contours are of the natural logarithm of the cooling or heating rate.) The air above the sample level experiences anomalous heating owing to the greater upward infrared flux from below the sample level. Both the warming and the cooling are larger in magnitude in the warmer atmosphere, again because of its larger infrared optical thickness.

It is also instructive to look at the response of the troposphere to an instantaneous reduction of specific humidity by 20% through the whole column, again starting from the RCE state as simulated by the SCM. This is shown in Figure 3.38.

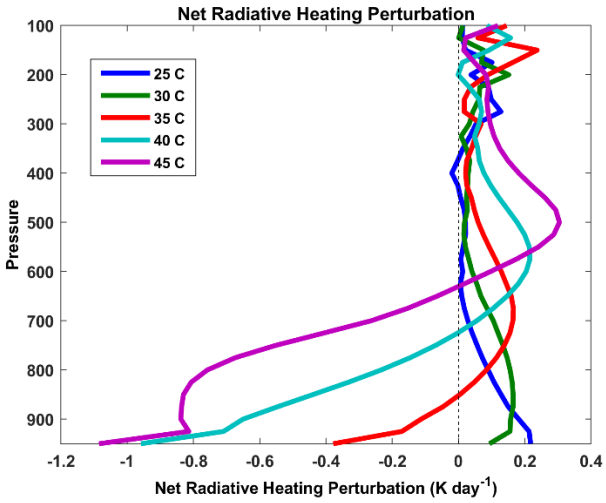

Figure 3.38: Perturbation net radiative heating rates in response to an instantaneous reduction of specific humidity of 20% through the whole troposphere, from the RCE states with SSTs ranging from 25 to 45°C. From Emanuel et al. (2014).

Note that for the lower SSTs, the column-integrated response to the drying is net heating, whereas this reverses for sufficiently high SSTs. At these higher SSTs, the negative response of column-heating to column drying is destabilizing, according to (3.85): negative values of $\hat{h}'$ would be associated with negative values of the column radiative cooling (first two terms on the right of (3.85)). This is does not lead to an exact criterion for instability owing to water vapor feedback alone, as we do not know, *a priori*, what the vertical structure of the drying is.

We can do a more legitimate test for stability by using our SCM in WTG mode, as described in section 3.3c. After running the SCM into RCE, we continue the integration but fix the temperature above the boundary layer…in this case, above 850 hPa and calculate at each mode level the vertical velocity necessary to hold the temperature constant. That vertical velocity is then used to vertically advect water vapor. In section 3.3c we specified perturbations to the RCE SST but here we hold the SST at its RCE value and add low amplitude noise. Details are described in Emanuel et al. (2014).

At relatively cool sea surface temperatures, the noise gradually dies away, but for SSTs above a critical value, somewhere in the range of 30-35 C, the single column transitions to one of two non-RCE equilibrium states: once with mean ascent and the other with mean descent. The

vertical profiles of vertical velocity and relative humidity of these two states are compared in Figure 3.39, and the RCE relative humidity profile is also shown for comparison.

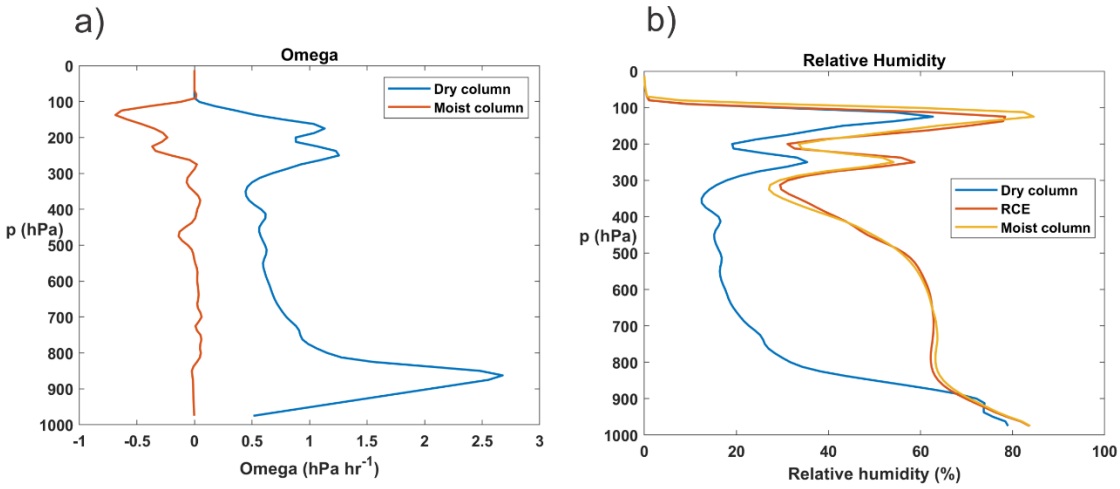

Figure 3.39: Vertical profiles of ω (a) and relative humidity (b) in the WTG single-column integrations starting from an RCE state with an RCE SST of 35.6 C. Blue curves show the subsiding column while red curves are for the ascending column. The RCE relative humidity profile is shown by the yellow curve in (b).

The asymmetry between the descending and ascending WTG solutions is striking, with much stronger departures from RCE in the descending column. Mass conservation would imply that the descending columns should occupy a small fractional area of the total domain, and this is indeed the case early in the self-aggregation process, at least in some cloud-permitting models (Wing et al., 2017). This has the effect of cooling the horizontal mean temperature above the boundary layer (essentially shifting the domain-mean RCE state itself), gradually favoring stronger ascent in the ascending columns, whose fractional area then shrinks. Eventually a balance is reached whereby the additional infrared emission in the dry regions balances the reduced emission from the convective clusters.

The destabilization of the RCE state by feedbacks involving radiation and surface fluxes is an important source of intraseasonal variability and is also important in driving tropical cyclones. We will have occasion to discuss self-aggregation again in our coming treatments of intraseasonal variability and tropical cyclones.

3.5 Tropical squall lines

On shorter space and time scales, deep convection is often organized into lines and arcs, as illustrated in Figures 3.5 and 3.6. In this case, the organization is brought about by the interaction of cold pools, produced by evaporating rain, with ambient wind shear.

The interaction of dry convection with background shear flows strongly favors convective rolls aligned with the shear vector (e.g. Kuo, 1963) and this is observed to be the case in laboratory experiments (e.g. Graham and Walker, 1933). But strong squall lines are observed to be oriented more nearly perpendicular to the low-level shear vector (Barnes and Sieckman, 1984; LeMone and G. M. Barnes, 1984), and this tends to be true outside the tropics as well

(Bluestein and Jain, 1985; Wyss and Emanuel, 1988). Tropical squall lines seem to be strongest when the shear is confined to low levels or is associated with a low-level jet with reversed shear above the jet (LeMone and G. M. Barnes, 1984).

An essential process in deep moist convection is the development of cold polls of air in the boundary layer, resulting from the evaporation of rain falling into the subcloud layer or through unsaturated air above the subcloud layer. The cold, dense air flows outward as a density current. In environments of low shear, such as classical RCE, the outflowing cold air eventually cuts off the supply of potentially unstable boundary layer air and the convective cell dies, as first documented by Byers and Braham (1948) based on results of one of the first field experiments designed to understand how deep convection works. The evolution of a typical deep convective cell in a low-shear environment is shown in Figure 3.40.

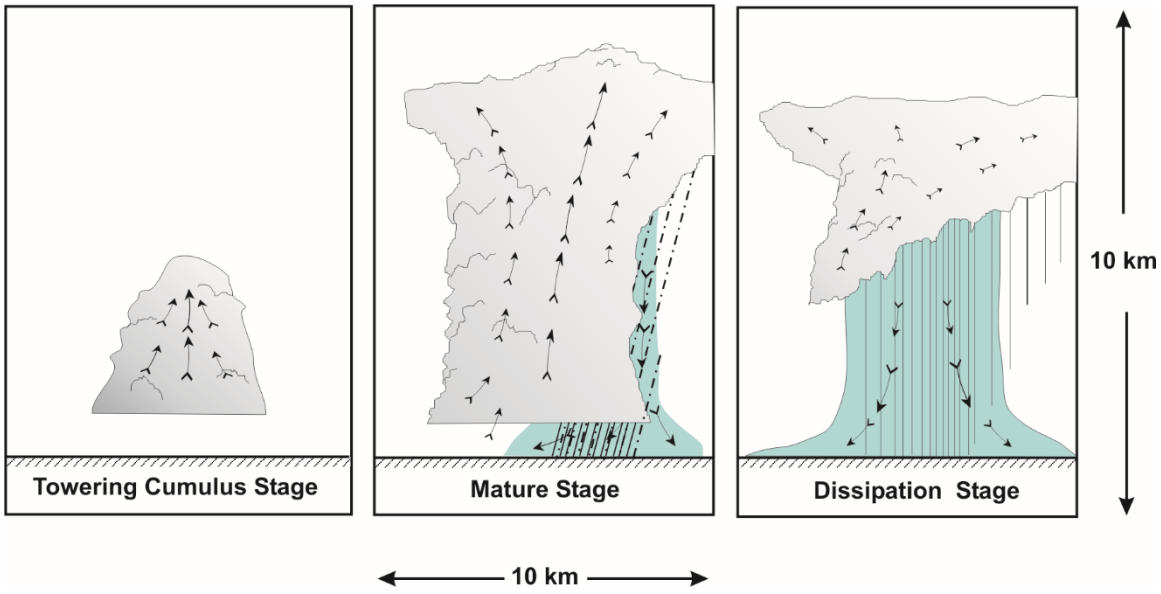

Figure 33.40: Evolution of a convective cell in a low-shear environment. In the earlies stages (left), an updraft develops in response to instability, but cloud droplets have not yet aggregated into precipitation. Later (center). precipitation forms and falls out, some if it evaporating in the subcloud layer and in unsaturated air above the subcloud layer. The cold, dense air begins (blue shading) to flow outward as a density current. Finally, the outflowing cold air cuts off the supply of potentially buoyant air at low levels, and the cell dissipates (right). The whole sequence may take 45 minutes to an hour.

However, if enough low-level shear is present, then the cold pool on the downshear side of the system will be inhibited from outrunning the deep convection aloft, and a quasi-two-dimensional squall line can thus persists somewhat longer, as theorized by Thorpe et al. (1982) and Rotunno et al. (1988) and illustrated in Figure 3.41. Following Rotunno et al. (1988), we show that there is an optimal magnitude of the low level shear for strong, persistent convection.

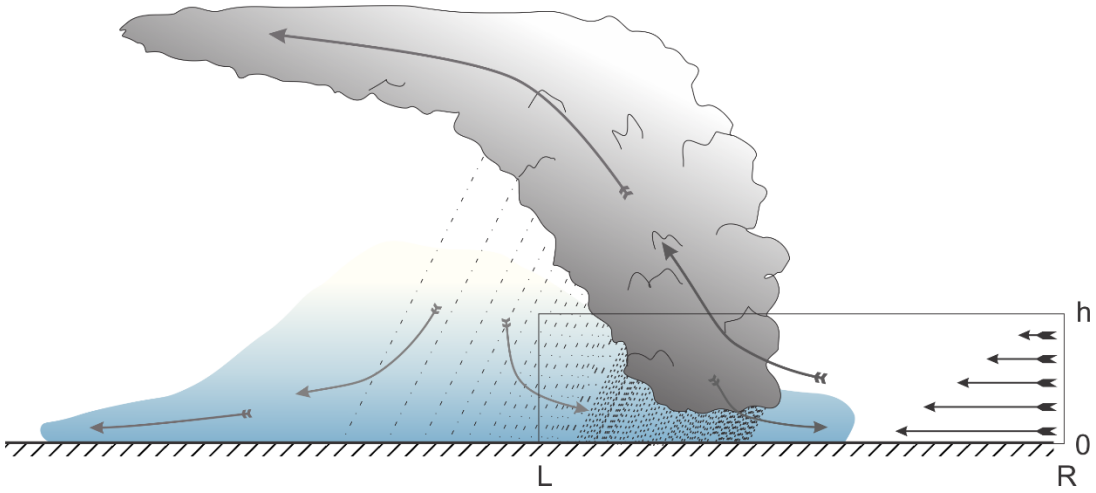

Figure 3.41: Schematic cross-section through a tropical squall line, in a frame of reference moving with the system from left to right. Gray arrows denote airflow and the straight black arrows at right show the ambient low-level shear flow relative to the squall line. The blue shading depicts downdraft air cooled by evaporation of falling precipitation and, at higher levels, melting of ice. The rectangular box in the lower right is a control volume described in the text.

We begin by defining η as the component of vorticity into the page, referring to Figure 3.41, and then write the conservation equation for η assuming that the flow is two-dimensional and Boussinesq at low levels:

$$\frac{\partial \eta}{\partial t} + \frac{\partial}{\partial x}\left(u\eta\right) + \frac{\partial}{\partial z}\left(w\eta\right) = -\frac{\partial B}{\partial x}, \tag{3.86}$$

where u and w are the components of velocity in the x and z directions, respectively, and B is the buoyancy, defined

$$B \equiv g\frac{T_v'}{\overline{T_v}}$$

in which T_v' is the departure of the virtual temperature from its unperturbed value ahead of the squall line, $\overline{T_v}$. By definition, then, $B = 0$ in the air out ahead of the squall line, on the right side of Figure 3.41. We now integrate (3.86) over the control volume indicated by the rectangle in the lower right of Figure 3.41. In doing this integral, we assume that the flow is steady, that there is no horizontal flow u on the left side of the box (denoted by L in the figure), and that the vertical velocity w vanishes at the surface. With these assumptions, integrating (3.86) over the area of the box yields

$$\int_0^h \left(u\eta\right)_R dz + \int_L^R \left(w\eta\right)_h dx = \int_0^h B_L dz. \tag{3.87}$$

If we further assume that the flow is strictly horizontal along the right edge of the box, then $\eta = \frac{\partial u}{\partial z}$ there and we can integrate the first term in (3.87):

$$\frac{1}{2}\left[u_0^2 - u_h^2\right]_L - \int_L^R w\eta \Big|_h dx = -\int_0^h B_L dz. \tag{3.88}$$

(Recall that the buoyancy, B_L , of the cold pool is negative, so the right side of (3.88) is positive.) Rotunno, Weiss, and Klemp (1988) contend that for strong, long-lived convection, the updraft must not emerge from the boundary layer with much vorticity η, else the updraft would be strongly tilted away from the vertical. If we further assume that there is no squall line-relative ambient flow in the cloud layer, that optimal conditions is

$$u_{0L}^2 = -2\int_0^h B_L dz. \tag{3.89}$$

Thus the colder the cold pool, the greater the difference in the square velocity between the boundary layer and the cloud layer is needed to meet the optimal condition (3.89).

If the flow is superoptimal from this point of view, we might expect the squall lines to form at an angle to the shear vector such that the cross-line flow is optimal. This is because shear along a two-dimensional disturbance has little or no effect on it, so there is no penalty to pay for rotating the orientation of the convection off an axis perpendicular the low-level shear.

It is possible to impose a background wind profile, including shear, on a cloud-permitting RCE simulation, by relaxing the horizontally averaged flow at each level toward a target wind speed. (A nice fringe benefit of doing so is the ability to back off the convective contribution to the vertical flux of horizontal momentum by keeping track of how much momentum has to be added to each layer to keep the mean wind field close to the target background wind.)

A series of numerical experiments was performed by Robe and Emanuel (2001), running a cloud-permitting model into and RCE state while driving the domain-average winds towards prescribed wind profiles. They ran the model on a 180 x 180 km domain with periodic boundary conditions and a horizontal grid spacing of 2 km, and forced the convection by imposing a constant radiative cooling rate of $5.4\ K\ day^{-1}$ from the surface to 13 km altitude[3]. Figure 3.42 shows snapshots of the updraft fields at 250 m altitude during the RCE states of three experiments, for three different prescribed background wind profiles. The left panel show the classical zero-mean-wind case; the middle panel shows a simulation in which a low-level shear of $6\ ms^{-1}$was imposed over the lowest 2 km, and the right panel shows the same but with a net shear of $10\ ms^{-1}$. In both the latter two cases, the shear vector points from right to left (opposite to the direction of the shear shown in Figure 3.41). In these simulations, the negative buoyancy of the cold pool increased with increasing imposed shear, so the right-hand side of (3.89) above is not independent of the specified background flow.

[3] The constant radiative cooling and the relatively small domain size prevented self-aggregation from occurring, though the phenomenon was relatively unknown at the time. The rate of imposed cooling was unrealistically large but hastened the approach to RCE.

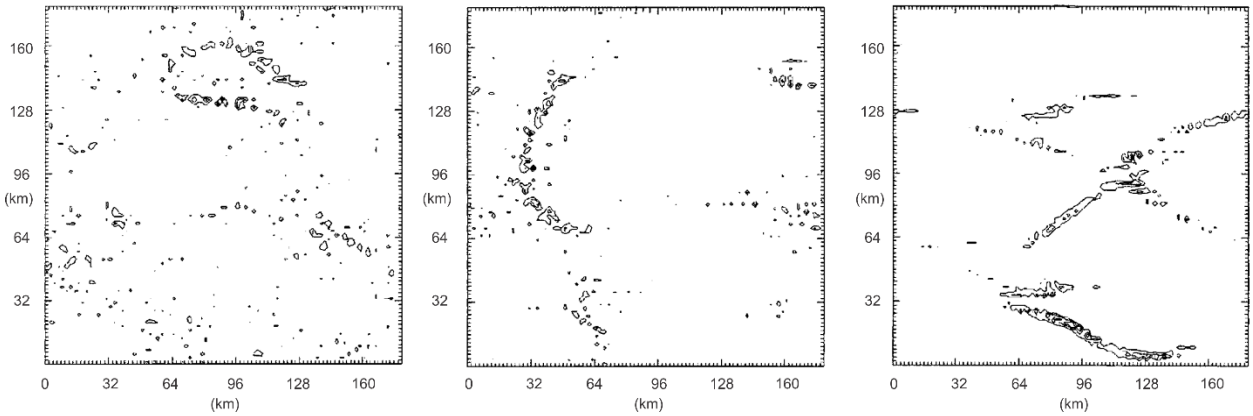

Figure 3.42: Snapshots of the updraft velocities at 250 m altitude from three simulations using a cloud-permitting model run into RCE states in a doubly-periodic domain. Left: No imposed background wind. Center and Right: $6\ ms^{-1}$ *and* $10\ ms^{-1}$*, respectively, of imposed background shear over the altitude range 0-2 km and directed left to right.*

In the classical RCE case with no imposed background shear (left panel of Figure 3.42), the convection is more or less random in space and time. In the simulation with moderate imposed low-level shear flow (center panel), the convection takes the form of arcs oriented across the shear vector and propagating downshear (right to left). The simulation with strong low-level shear (right panel) shows convection aligned at angles to the imposed shear, and also propagating downshear.

Other experiments not shown here also exhibit impressive squall-line organization with the shear vector rotates, or even reverses with altitude. If mono-directional shear extends through too deep a layer, the convection becomes organized along rather than across the shear vector.

These experiments also showed that the convective momentum flux is broadly down-gradient, but is not closely related to the local shear. The non-local nature of the convective momentum flux is consistent with results derived from observations of tropical squall lines by LeMone et al. (1984).

We shall return to the subject of the spatial and temporal organization of moist convection in our discussion of boundary layer convection in the next chapter.

References

Arakawa, A., and W. H. Schubert, 1974: Interaction of a cumulus cloud ensemble with the large-scale environment, part I. *J. Atmos. Sci.*, **31,** 674-701.

Barnes, G. M., and a. K. Sieckman, 1984: The environment of fast- and slow-moving tropical mesoscale convective cloud lines. *Mon. Wea. Rev.***,** 112.

Bluestein, H. B., and a. M. H. Jain, 1985: Formation of mesoscale lines of precipitation: Severe squall lines in Oklahoma during the spring. *J. Atmos. Sci.*, **42,** 1711-1732.

Bony, S., and K. A. Emanuel, 2001: A parameterization of the cloudiness associated with cumulus convection: Evaluation using toga coare data. *J. Atmos. Sci.*, **58,** 3158-3183.

Bretherton, C. S., and a. P. K. Smolarkiewicz, 1989: Gravity waves, compensating subsidence and detrainment around cumulus clouds. *J. Atmos.. Sci.*, **46,** 740-759.

Bretherton, C. S., P. N. Blossey, and M. F. Khairoutdinov, 2005: An energy-balance analysis of deep convective self-aggregation above uniform sst. *J. Atmos. Sci.*, **62,** 4273-4292.

Byers, H. R., and R. R. Braham, Jr., 1948: Thunderstorm structure and circulation. *J. Meteor.*, **5,** 71-86.

Cronin, T., and K. A. Emanuel 2013: The climate time scale in the approach to radiative-convective equilibrium. *J. Adv. Model. Earth Sys.*, **5**, doi:10.1002/jame.20049.

Emanuel, K., A. A. Wing, and E. M. Vincent, 2014: Radiative-convective instability. *J. Adv. Model. Earth Sys.*, **5,** 1-14, doi::10.1002/2013MS000269.

Emanuel, K. A., 1993: The effect of convective response time on WISHE modes. *J. Atmos.. Sci.*, **50,** 1763-1775.

Emanuel, K. A., and M. Živkovic-Rothman, 1999: Development and evaluation of a convection scheme for use in climate models. *J. Atmos. Sci.*, **56,** 1766-1782.

Graham, A., and G. T. Walker, 1933: Shear patterns in an unstable layer of air. *Philosophical Transactions of the Royal Society of London. Series A, Containing Papers of a Mathematical or Physical Character*, **232,** 285-296, doi:doi:10.1098/rsta.1934.0008.

Held, I. M., R. S. Hemler, and V. Ramaswamy, 1993: Radiative-convective equilibrium with explicit two-dimensional moist convection. *J. Atmos. Sci.*, **50,** 3909-3927, doi:10.1175/1520-0469(1993)050<3909:Rcewet>2.0.Co;2.

Khairoutdinov, M. F., and D. A. Randall, 2003: Cloud resolving modeling of the arm summer 1997 iop: Model formulation, results, uncertainties and sensitivities. *J. Atmos. Sci.*, **60,** 607-625.

Kuo, H. L., 1963: Perturbations of plane Couette flow in stratified fluid and origin of cloud streets. *The Physics of Fluids*, **6,** 195-211, doi:10.1063/1.1706719.

LeMone, M. A., G. M. Barnes, and E. J. Zipser, 1984: Momentum flux by lines of cumulonimbus over the tropical oceans. *J. Atmos.. Sci.*, **41,** 1914-1932.

LeMone, M. A., and E. J. S. G. M. Barnes, and E. J. Zipser, 1984: The tilt of the leading edge of mesoscale tropical convective lines. *Mon. Wea. Rev.*, **112,** 510-519.

Manabe, S., and R. F. Strickler, 1964: On the thermal equilibrium of the atmosphere with convective adjustment. *J. Atmos. Sci.*, **21,** 361-385.

Manabe, S., J. Smagorinsky, and R. F. Strickler, 1965: Simulated climatology of a general circulation model with a hydrologic cycle. *Mon. Wea. Rev.*, **93,** 769-798.

Manabe, S., and R. T. Wetherald, 1967: Thermal equilibrium of the atmosphere with a given distribution of relative humidity. *J. Atmos. Sci.*, **24,** 241-259, doi:10.1175/1520-0469(1967)024<0241:teotaw>2.0.co;2.

Morcrette, J.-J., 1991: Radiation and cloud radiative properties in the european centre for medium-range weather forecasts forecasting system. *J. Geophys. Res.*, **96,** 9121-9132.

Morton, B. R., G. I. Taylor, and J. S. Turner, 1956: Turbulent gravitational convection from maintained and instantaneous sources. *Proc. Roy. Soc. London*, **A234,** 1-23.

Neelin, J. D., and I. M. Held, 1987: Modeling tropical convergence based on the moist static energy budget. *Mon. Wea. Rev.*, **115,** 3-12.

Paluch, I. R., 1979: The entrainment mechanism in colorado cumuli. *J. Atmos. Sci.*, **36,** 2462-2478.

Pauluis, O., and I. M. Held, 2002: Entropy budget of an atmosphere in radiative-convective equilibrium. Part I: Maximum work and frictional dissipation. *J. Atmos. Sci.*, **59,** 125-139.

Robe, F. R., and K. Emanuel, 2001: The effect of vertical wind shear on radiative-convective equilibrium states. *J. Atmos. Sci.*, **58,** 1427-1445.

Rotunno, R., J. B. Klemp, and M. L. Weisman, 1988: A theory for strong, long-lived squall lines. *J. Atmos. Sci.*, **45,** 463-485.

Schmidt, W., 1941: Turbulent propagation of a stream of heated air. *Z. angew. Math. Mech.*, **21,** 265-351.

Singh, M. S., and P. A. O'Gorman, 2015: Increases in moist-convective updraught velocities with warming in radiative-convective equilibrium. *Quart. J. Roy. Meteor. Soc.*, **141,** 2828-2838, doi:10.1002/qj.2567.

Sobel, A. H., and C. S. Bretherton, 2000: Modeling tropical precipitation in a single column. *J. Climate*, **13,** 4378-4392, doi: 10.1175/1520-0442(2000)013<4378:Mtpias>2.0.Co;2.

Thorpe, A. J., M. J. Miller, and M. W. Moncrieff, 1982: Two-dimensional convection in non-constant shear: A model of mid-latitude squall lines. *Quart. J. Roy. Meteor. Soc.*, **108,** 739-762.

Tompkins, A. M., and G. C. Craig, 1998: Radiative–convective equilibrium in a three-dimensional cloud-ensemble model. *Quart. J. Roy. Meteor. Soc.*, **124,** 2073-2097, doi:doi:10.1002/qj.49712455013.

Wing, A. A., and K. A. Emanuel, 2014: Physical mechanisms controlling self-aggregation of convection in idealized numerical modeling simulations. *J. Adv. Model. Earth Sys.*, **6,** 75-90, doi::10.1002/2013MS000270.

Wing, A. A., and T. W. Cronin, 2016: Self-aggregation of convection in long channel geometry. *Quart. J. Roy. Meteor. Soc.*, **142,** 1-15, doi:10.1002/qj.2628.

Wing, A. A., K. Emanuel, C. E. Holloway, and C. Muller, 2017: Convective self-aggregation in numerical simulations: A review. *Surv. Geophys.*, doi: 10.1007/s10712-017-9408-4.

Wyss, J., and a. K. A. Emanuel, 1988: The pre-storm environment of midlatitude prefrontal squall lines. *Mon. Wea. Rev.*, **116,** 790-794.

Xu, K.-M., and K. A. Emanuel, 1989: Is the tropical atmosphere conditionally unstable? *Mon. Wea. Rev.*, **117,** 1471-1479.

Zhang, M. H., and J. L. Lin, 1997: Constrained variational analysis of sounding data based on column-integrated budgets of mass, heat, moisture, and momentum: Approach and application to arm measurements. *J. Atmos. Sci.*, **54,** 1503-1524, doi:10.1175/1520-0469(1997)054<1503:cvaosd>2.0.co;2.